

# Forensic reconstruction of galaxy colour evolution and population characterisation

Matías Bravo<sup>1</sup>★, Aaron S. G. Robotham<sup>1,2</sup>, Claudia del P. Lagos<sup>1,2,3</sup>,  
Luke J. M. Davies<sup>1</sup>, Sabine Bellstedt<sup>1</sup> and Jessica E. Thorne<sup>1</sup>

<sup>1</sup>*International Centre for Radio Astronomy Research (ICRAR), M468, University of Western Australia, 35 Stirling Hwy, Crawley, WA 6009, Australia.*

<sup>2</sup>*ARC Centre of Excellence for All Sky Astrophysics in 3 Dimensions (ASTRO 3D).*

<sup>3</sup>*Cosmic Dawn Center (DAWN).*

Accepted XXX. Received YYY; in original form ZZZ

## ABSTRACT

Mapping the evolution of galaxy colours, from blue star-forming to red passive systems, is fundamental to understand the processes involved in galaxy evolution. To this end, we reconstruct the colour evolution of low-redshift galaxies, combining stellar templates with star formation and metallicity histories of galaxies from the Galaxy And Mass Assembly survey and SHARK semi-analytic model. We use these colour histories to robustly characterise the evolution of red and blue galaxy populations over cosmic time. Using a Gaussian Mixture Model to characterise the colour distribution at any given epoch and stellar mass, we find both observations and simulations strongly favour a model with only two populations (blue and red), with no evidence for a third "green" population. We map the evolution of mean, weight, and scatter of the blue and red populations as a function of both stellar mass and lookback time. Using our simulated galaxy catalogue as a testbed, we find that we can accurately recover galaxies colour histories up to a lookback time of  $\sim 6$  Gyr. We find that both populations show little change in the mean colour for low-mass galaxies, while the colours at the massive end become significantly redder with time. The stellar mass above which the galaxy population is predominantly red decreases by 0.3 dex in the last 5 Gyrs. We find a good agreement between observations and simulations, with the largest tension being that massive galaxies from SHARK are too blue (a known issue with many galaxy evolution models).

**Key words:** galaxies: evolution – software: simulations – techniques: photometric

## 1 INTRODUCTION

Galaxies in the Local Universe display a bimodal distribution in observed optical colours (e.g., Strateva et al. 2001; Hogg et al. 2002; Blanton et al. 2003; Baldry et al. 2004, 2006; Driver et al. 2006), with a well-defined low-scatter "red" population (the so-called "red sequence") and a broader "blue" population (known as the "blue cloud"). When colours are corrected for dust reddening, which confuses intrinsically red galaxies with blue but dust-obscured galaxies, this bimodality becomes even more striking (Taylor et al. 2015, hereafter T15). This bimodality also shows a marked dependency on stellar mass, with a higher fraction of massive galaxies being red (e.g., Baldry et al. 2004; Peng et al. 2010; T15), and a secondary dependence on the environment, where galaxies in low-density environments are more commonly blue (e.g., Kauffmann et al. 2004; Baldry et al. 2006; Peng et al. 2010; Davies et al. 2019b). How-

ever, these populations do not retain the same characteristics with redshift, as the global distribution of galaxies becomes bluer and the dominance of the blue cloud increases with lookback time (e.g., Wolf et al. 2003; Bell et al. 2004; Williams et al. 2009). Conversely, red galaxies are typically more massive and become a larger fraction of the total galaxy population with time, which implies that galaxies form blue and at some point become red as the universe evolves (e.g., Faber et al. 2007). A fundamental goal for understanding galaxy evolution is explaining how and why this change from blue to red takes place.

For the intrinsic colour of a galaxy to be red, it requires the absence of blue stars, which have far shorter lifespans than their red counterparts (e.g., Schaller et al. 1992). This happens when a galaxy has stopped forming stars long enough that the last blue stars have exhausted themselves and only the red stars remain. This process of star formation slowing down and finally ceasing is commonly referred to as "quenching" (e.g., Blanton 2006; Borch et al. 2006; Faber et al. 2007; Fang et al. 2013; Moustakas et al. 2013; Peng et al.

★ E-mail: matias.bravo@icrar.org

2015), which occurs when galaxies no longer have a ready supply of gas for star formation. There are a variety of physical processes that can facilitate the quenching process, such as active galactic nuclei (AGN) feedback (e.g., Springel et al. 2005; Bower et al. 2006; Croton et al. 2006; Hopkins et al. 2006; Somerville et al. 2008), supernovae feedback (e.g., Springel et al. 2005; Dalla Vecchia & Schaye 2012; Lagos et al. 2013), ram-pressure stripping (e.g., Crowl et al. 2005; Machacek et al. 2006; Kawata & Mulchaey 2008; McCarthy et al. 2008) or strangulation (e.g., Balogh et al. 2000; Kereš et al. 2005; Dekel & Birnboim 2006; Peng et al. 2015). While we have a good understanding of these mechanisms, in practice we know very little about which mechanism dominates the quenching of galaxies in specific populations as defined by e.g. morphology, environment or stellar mass, and how the prevalence of these processes changes with time. As such, the astrophysical mechanisms that drive galaxies to transition from the blue cloud to the red sequence, and their prevalence as a function of other galaxy properties is far from clear (e.g., Barro et al. 2013; Wetzel et al. 2013; Schawinski et al. 2014; Wheeler et al. 2014; Yesuf et al. 2014; Fossati et al. 2017; Hahn et al. 2017; Smethurst et al. 2018; Anghopo et al. 2019; Belli et al. 2019; Trussler et al. 2020; Wild et al. 2020; Belli et al. 2021; Kalinova et al. 2021; Zhang et al. 2021).

The region between the red and blue populations, which is commonly referred to as the "green valley", is sparsely populated (e.g., Martin et al. 2007; Wyder et al. 2007). This has been suggested as evidence that, whichever mechanisms are responsible for transforming galaxies from blue to red, must be rapid (relative to cosmic timescales, e.g., Schawinski et al. 2014; Bremer et al. 2018). Results from simulations however suggest that different quenching mechanisms have different timescales, such as stellar feedback being significantly slower than AGN feedback or environmental effects ( $\sim 4$  Gyr compared to  $\sim 2$  Gyr, e.g., Trayford et al. 2016; Nelson et al. 2018; Wright et al. 2019). Hence, the study of the timescales of these colour changes, from an observational perspective can provide unique constraints on the physical mechanisms behind star formation quenching.

Although we can observe and measure the colours of different galaxy populations at different lookback times, the inference of the colour transformation of galaxies is difficult, as it is unclear how to connect the observed properties across cosmic time. In particular, a major challenge is how to connect red galaxies to their blue progenitors, avoiding the effects of progenitor bias (e.g., van Dokkum & Franx 1996; Kaviraj et al. 2009; Belli et al. 2015). Instead of trying to establish a connection between galaxy samples at different cosmic times, another possible approach would be to reconstruct the evolutionary history of a given sample. This evolution is encoded in the light emitted by its stars, which can be extracted with the use of spectral energy distribution (SED) fitting techniques (e.g., da Cunha et al. 2008; Noll et al. 2009; Han & Han 2014; Chevallard & Charlot 2016; Iyer & Gawiser 2017; Leja et al. 2017; Carnall et al. 2018; Boquien et al. 2019; Robotham et al. 2020). These methods require the use of single stellar population (SSP) spectral templates and of stellar initial mass function (IMF) to model the stellar light emission, plus models for other physical processes like dust attenuation and re-emission.

To limit the number of free parameters required for SED fitting, some model is also required for the star formation history of the galaxy (SFH), which restricts the possible combination of stellar templates. SFH models are commonly divided between those that assume a given functional form for the SFH (referred to as "parametric") and those that instead divide the SFH in discrete bins of cosmic time ("non-parametric"). While highly desirable,

the inclusion of an evolving gas-phase metallicity (metallicity history, ZH) is uncommon in SED fitting tools and more so its use in the literature (to the authors' knowledge, only in Robotham et al. 2020; Bellstedt et al. 2020b, 2021; Thorne et al. 2021). Allowing for this is physically well-motivated, as the existence of the stellar mass-star formation-metallicity plane indicates that the metallicity of a galaxy will change as they grow (e.g., Mannucci et al. 2010; Lara-López et al. 2010, 2013; Brown et al. 2016, 2018; Bellstedt et al. 2021). This will lead to different SSP templates being used, compared to assuming a fixed metallicity, which will affect the predicted colour evolution and therefore on the colour transition timescales. Under the assumption that the IMF does not evolve with time (e.g., Kroupa 2001; Chabrier 2003), the fitted SFH and ZH combined with the chosen IMF and SSP templates then offer a straightforward reconstruction of the intrinsic galaxy SED at any point backwards in time. In the particular case of inferring colour transition timescales, a parametric model for the SFH is highly desirable, as a non-parametric SFH may not offer the required time resolution.

In this work we make use of the Galaxy And Mass Assembly (GAMA; Driver et al. 2011; Liske et al. 2015) survey and the SHARK semi-analytic model (SAM) of galaxy formation (Lagos et al. 2018, hereafter L18) to reconstruct the colour evolution of galaxies using SED fitting. In particular, we aim to answer the following question:

(i) how have the colours of the local blue and red galaxy populations evolved with time?

This is critical to understand the timescales on which galaxies transition from the blue cloud to the red sequence (the subject of a future paper; Bravo et al. in preparation).

There are also three other important and related questions that we must first address to answer the above:

(ii) how well we can reconstruct the colour evolution of galaxies from their panchromatic SEDs?

(iii) how can we best define the blue and red populations across cosmic time?

(iv) is the green valley the superposition of the blue and red populations, or a third population on its own?

The use of simulations to answer question (ii) is crucial, as they offer a test-bed for our reconstruction techniques and a way of identifying and quantifying their limitations. The best approach is to characterise the galaxy populations in both observations and simulations with the same technique and quantify the differences. Although the presence of two colour populations is well documented, there is no clear agreement across literature examples on a quantitative definition (Bell et al. 2003; Baldry et al. 2004; Peng et al. 2010; Taylor et al. 2015; Trayford et al. 2016; Bremer et al. 2018; Nelson et al. 2018; Wright et al. 2019).

This is especially critical, as the details of the adopted methodology can have a strong effect when inferring the colour transition timescales. Strongly connected to this is the nature of the "green valley", as a third "green" population is also to be any quantitative description of both blue and red populations will change of a third "green" population. Evidence suggests that it is not a population of its own, but the overlap of the blue and red populations (e.g., Schawinski et al. 2014; Taylor et al. 2015). However, it is worth exploring again, using our exact methodology, whether we find evidence of a third population across cosmic time. Finally, as we recreate the colour evolution of galaxies in simulations, we also test how well theoretical models reproduce the inferred colour evolution. While predictions have been made from simulation for the colour evolution

and colour transition timescales (e.g., Trayford et al. 2016; Nelson et al. 2018; Wright et al. 2019), direct comparisons with equivalent observational results have not been attempted.

The rest of this work is ordered as follows. We describe the data used in this work in Section 2. Using this data, we present our method to study the colour evolution in Section 3. We discuss the results presented in this work in Section 4. Finally, we summarise the findings of this work in Section 5. In this work, we adopt the Planck Collaboration et al. (2016)  $\Lambda$ CDM cosmology, with values of matter, baryon, and dark energy densities of  $\Omega_b = 0.0488$ , and  $\Omega_\Lambda = 0.6879$ , respectively, and a Hubble parameter of  $H_0 = 67.51 \text{ km s}^{-1} \text{ Mpc}^{-1}$ .

## 2 GALAXY CATALOGUES

In this work, we use the same galaxy sample presented in Bellstedt et al. (2020b, hereafter B20b), together with a similarly selected sample of galaxies from SHARK.

### 2.1 Observed catalogues (GAMA)

GAMA is a spectroscopic redshift survey that targeted  $\sim 300,000$  galaxies in five fields (total of  $\sim 285 \text{ deg}^2$ ), selecting galaxies with  $r_{\text{ap}} < 19.8$  (save one field, G23, selected with  $i_{\text{ap}} < 19.0$ ), for which achieved  $\sim 98\%$  completeness.

From this survey, we combine the most recent version of the GAMA redshift catalogue (Liske et al. 2015) with the galaxy property catalogue derived from SED fitting by B20b, which used the latest photometry available from Bellstedt et al. (2020a). The use of the B20b sample limits the available fields from five to the three equatorial (G09, G12 and G15,  $\sim 180 \text{ deg}^2$ ). From this point, we will refer to this data set as GAMA.

Briefly, the majority ( $\sim 85\%$ ) of the GAMA redshifts were measured using the AAOmega spectrograph (Saunders et al. 2004; Sharp et al. 2006) and the Two-degree Field (2dF; Lewis et al. 2002) fibre plate on the Anglo-Australian Telescope (AAT). These redshifts were obtained by cross-correlating the observed spectra with spectral templates using the AUTOZ software (Baldry et al. 2014). The remaining redshifts were collected from previous surveys covering the GAMA footprint (see Liske et al. 2015 for a detailed description). All redshifts were then assigned a quality flag ( $nQ$ ), ranging from 0 (worst) to best (4), with  $\sim 90\%$  of the galaxies with  $nQ \geq 3$ .

The new photometry catalogue by Bellstedt et al. (2020a) was built from GALEX+VST+VISTA+WISE+Herschel (Martin et al. 2005; Arnaboldi et al. 2007; Wright et al. 2010; Pilbratt et al. 2010; Sutherland et al. 2015) imaging, using the software ProFOUND (Robotham et al. 2018). A combination of  $r$  and  $Z$  filters were used for source finding, with the photometry measured using the segments defined during source finding for bands FUV to W2, and the positions of these segments for PSF photometry from W3 to S500. B20b then combined this new photometry catalogue with the existing redshifts to perform SED fitting on a sub-sample of the survey (galaxies with  $nQ \geq 3$ ,  $z < 0.06$  and  $r < 19.5^1$ ) to recover galaxy properties and star formation/metallicity histories (SFH/ZH). This was done using ProSPECT<sup>2</sup> (Robotham et al. 2020), a high-level

SED generator, whose design has influences from existing spectral fitting codes like MAGPHYS (da Cunha et al. 2008) and CIGALE (Noll et al. 2009; Boquien et al. 2019). ProSPECT uses a combination of either the GALAXEV (Bruzual & Charlot 2003) or E-MILES (Vazdekis et al. 2016) Stellar Population Synthesis (SSP) libraries with the Charlot & Fall (2000) multi-component dust attenuation model and the Dale et al. (2014) dust re-emission templates, under the assumption of a Chabrier (2003) Initial Mass Function (IMF).

From the wide variety of choices of functional forms for the characterisation of the star formation and metallicity histories (SFH and ZH, respectively) that ProSPECT offers, B20b used:

- the GALAXEV SSP library.
- `massfunc_snorm_trunc`, a parametric description of the SFH using a skewed and truncated Gaussian distribution, as the functional form for the SFH, with  $m_{\text{SFR}}$ ,  $m_{\text{mpeak}}$ ,  $m_{\text{mperiod}}$ , and  $m_{\text{mskew}}$  as free parameters to fit.
- `Zfunc_massmap_lin`, a linear map between the metallicity increase and the stellar mass growth, to parameterise the ZH, fitting  $Z_{\text{final}}$ , the final metallicity.
- $\tau_{\text{birth}}$ ,  $\tau_{\text{screen}}$ ,  $\alpha_{\text{birth}}$  and  $\alpha_{\text{screen}}$  dust parameters as free parameters within the fitting.
- $\text{pow}_{\text{birth}} = \text{pow}_{\text{screen}} = -0.7$ , the default value in ProSPECT.
- 13.4 Gyr as the maximum age for star formation, demanding that stars form after  $z \sim 11$ .

To fit the parameters, B20b used a Covariance Matrix Adaptation genetic algorithm to make an initial estimate of the parameter. Then a Component-wise Hit And Run Metropolis Markov-Chain Monte Carlo algorithm was used with 10,000 steps to determine the best-fitting SFH, ZH and dust parameters. While the observed colours from GAMA are affected by noise, this noise is taken into account in the SED fitting process (i.e., all intrinsic colours are noiseless by construction). This means that the intrinsic colours recovered with ProSPECT are robust against this noise and that it is fair to compare them to the results directly from our simulations. For the rest of this work, we will refer to the sample of galaxies from B20b as simply GAMA.

### 2.2 Simulated catalogues (SHARK)

In this work, we use the semi-analytic model (SAM) SHARK (L18), which has been shown to reproduce a wide variety of observations (Amarantidis et al. 2019; Davies et al. 2019a; Lagos et al. 2019, 2020; Chauhan et al. 2019, 2020, 2021; Bravo et al. 2020). Most critical for this work are the excellent predictions of observed number counts, luminosity functions (Lagos et al. 2019, 2020) and low-redshift colour distributions (Bravo et al. 2020). Briefly, a SAM generates and evolve galaxies using dark matter (DM) only N-body simulations, by following a set of equations that described the relevant physical processes to galaxy evolution. What follows is a brief description of the base DM-only simulation, SHARK, and how we generate in post-process the SEDs for these simulated galaxies using ProSPECT.

For this work we use the SURFS suite of DM-only simulations (Elahi et al. 2018), which adopts a  $\Lambda$ CDM (Planck Collaboration et al. 2016) cosmology and span a range of box length of 40 – 210  $h^{-1} \text{ cMpc}$  ( $\text{cMpc}$  being comoving megaparsec) and particle mass of  $4.13 \times 10^7$  to  $5.90 \times 10^9$ , reaching up to 8.5 billion particles. This simulation suite was run with a memory lean version of the GADGET2 code on the Magnus supercomputer at the Pawsey Supercomputing Centre. We use the same simulation as in L18, L210N1536, with a box size of 210  $h^{-1} \text{ cMpc}$ ,  $1,536^3$  DM particles, a particle

<sup>1</sup> The new photometry catalogue moved the 95% completeness from  $r < 19.8$  to  $r < 19.5$ .

<sup>2</sup> <https://github.com/asgr/ProSpect>

mass of  $2.21 \times 10^8 h^{-1} M_{\odot}$ , and a softening length of  $4.5 h^{-1} \text{ckpc}$ . SURFS produced 200 snapshots for each simulation, with a typical time-span between snapshots in the range of  $\sim 6 - 80$  Myr. The halo catalogues for the SURFS suite were constructed using the 6D FoF finder VELOCIRAPTOR (Poulton et al. 2018; Cañas et al. 2019; Elahi et al. 2019a), and for the halo merger trees TREEFROG (Elahi et al. 2019b) was used. We refer the reader to L18 for more details on the construction of the merger trees and halo catalogues used in this work.

These catalogues are the input for SHARK, which populates these halo catalogues with galaxies and evolves them following prescriptions for key physical processes that shape the formation and evolution of galaxies. Among these processes are the collapse and merging of DM haloes, gas accretion to both halo and galaxy, star formation, black hole growth, feedback by stellar and AGN, galaxy mergers, disc instabilities and environmental processes affecting the gas supply of satellite galaxies. Most of these processes can be modelled by a choice of different prescriptions built into SHARK, in this work we use the prescription and parameter choices from L18 (see their table 2). Important for this work is that SHARK adopts the same universal Chabrier (2003) IMF as used in ProSPECT. The model presented in L18 has been calibrated only to reproduce the  $z = 0, 1, 2$  stellar mass functions (SMFs), the  $z = 0$  black hole–bulge mass relation and the mass–size relation.

To construct the GAMA-like sample, we first need to generate synthetic SEDs for the SHARK galaxies to replicate the  $r_{\text{ap}} < 19.8$  selection. For this, we start with the SFH and ZH of the galaxies, contained in the `star_formation_histories` output file from SHARK<sup>3</sup>. These files contain the information for each of the three channels for star formation (in disc, in bulge due to mergers, and in bulge due to disc instabilities).

We use VIPERFISH<sup>4</sup>, a light wrapper around ProSPECT, to generate the SEDs. From the discretely-valued SFH and ZH at the observation snapshot, it first calculates the stellar light emission for each galaxy. Next, it accounts for dust screening and re-emission, where young stars (age less than 10 Myr) are attenuated by the dust in birth clouds, and then all stars are attenuated by the diffuse interstellar medium (ISM). While ProSPECT currently includes several models to account for the AGN contribution to the SEDs, with the Fritz et al. (2006); Feltre et al. (2012) model, in particular, providing a good match to existing observations (Thorne et al. in preparation), we do not attempt to include this effect in SHARK. We note also that this is a recent addition (Thorne et al. in preparation), and therefore B20b did not include an AGN component in their analysis (also justified by the negligible occurrence of AGN at such low redshift). We leave how to connect the central black hole properties in SHARK to the AGN SEDs in ProSPECT for future work.

Following Lagos et al. (2019); Bravo et al. (2020), we use their parameterisation model for dust<sup>5</sup>, which uses the best-fit dust fraction-to-gas metallicity ratio from Rémy-Ruyer et al. (2014) to calculate  $\Sigma_{\text{dust}}$ , and then apply the Charlot & Fall (2000) parameters  $\Sigma_{\text{dust}}$ -dependency found in Trayford et al. (2020). For a more detailed description, we refer the reader to Sections 2.1 and 3.1 of Lagos et al. (2019).

The GAMA sample from B20b was chosen to be a volume-

limited sample, which means that creating a synthetic lightcone is not required to reproduce this sample. Instead, we choose our galaxies directly from one of the simulation snapshots, specifically snapshot 195 ( $z = 0.0668$ ). We select galaxies by the GAMA magnitude selection of  $r < 19.8$ , for which all galaxies in the box are assumed to be at the redshift of the snapshot. As we will also fit these galaxies with ProSPECT (see next subsection), due to the computational cost of SED generation and fitting we are not able to use the full simulation box to draw a galaxy sample. For parallelisation purposes, the merger trees from the simulation are provided divided into 64 "subvolumes", with each one yielding roughly the same number of GAMA-like galaxies as in our GAMA sample. We choose to use five random subvolumes in this work, to balance between the effect of large-scale structure variations across subvolumes and the computational cost of SED generation and fitting. This yields a total sample of  $\sim 30,000$  GAMA-like galaxies, five times more than our observations and  $\sim 50$  times more than that used by Robotham et al. (2020).

### 2.3 Fitted simulations (SHARK<sub>fit</sub>)

Of special interest for this work is how the reconstructed colour evolution from observational data is informed by the SED modelling choices built into ProSPECT. In particular, the assumption of a skewed Normal functional form for the SFH and of a linear map from the mass growth to the ZH. For this purpose, we also fitted the synthetic SEDs generated for SHARK with ProSPECT, in a comparable (but not equal) manner to B20b.

We assume the same functional forms for the SFH and ZH (`massfunc_snorm_trunc` and `Zfun_massmap_lin`) but modify the priors for the dust parameters. We set a log-Uniform prior for both opacities, with  $-6 < \{\log_{10}(\tau_{\text{BC}}), \log_{10}(\tau_{\text{ISM}})\} < \log_{10}(5)$ , which matches the range of opacities used to generate the SEDs for SHARK (instead of the narrower  $-2.5$  to  $1$  range used by B20b and Thorne et al. 2021). The dust temperature parameters ( $\alpha_{\text{BC}}$  and  $\alpha_{\text{ISM}}$ ) are fixed to 1 and 3, respectively, as per the generative SHARK SEDs (B20b and Thorne et al. 2021 used a Gaussian prior of mean 2 and standard deviation of 1). Finally, we use the same log-Uniform prior for  $Z_{\text{final}}$  as B20b and Thorne et al. (2021), in the range  $-4 < \log_{10}(Z_{\text{final}}) < -1.3$ . For the photometry errors, we have assumed a fixed signal-to-noise ratio of 10 across all bands (i.e., error of  $\sim 0.1$  mag), as we found this to provide the most accurate stacked SFH recovery. We note that we required a much larger number of fitting steps compared to B20b and Thorne et al. (2021) for these fits ( $\sim 30$  times the total number of steps, see Appendix A for further discussion).

Figure 1 compares the stellar mass and intrinsic colour of SHARK galaxies to the best fit results, at the redshift of observation ( $z = 0.0668$ ). In line with the results from Robotham et al. (2020) (see their figure 30), we see a superb recovery of the stellar masses, with a negligible global bias ( $\sim -0.03$  dex) and very small global scatter ( $\sim 0.08$  dex). The running percentiles also show that this remains true across all stellar masses. Globally, the colour recovery also shows a very small bias ( $\sim 0.04$  mag), with a small scatter ( $\sim 0.15$  mag), though unlike stellar masses the recovery does show some evolution with colour. While it is interesting to note that both bias and scatter reach a maximum halfway between the density peaks of the blue and red populations (at  $\sim 1$  and  $\sim 2$  mag, respectively), their scale still reflects a high-quality recovery of the intrinsic SHARK colours.

We find that the recovery of the stacked SFH is less optimal, with a lower peak and flatter decline (see Appendix A). While we

<sup>3</sup> This is done by setting `output_sf_histories = true` on the SHARK configuration file.

<sup>4</sup> <https://github.com/asgr/Viperfish>

<sup>5</sup> Called EAGLE- $\tau$  RR14 in Lagos et al. (2019), and T20-RR14 in Bravo et al. (2020).



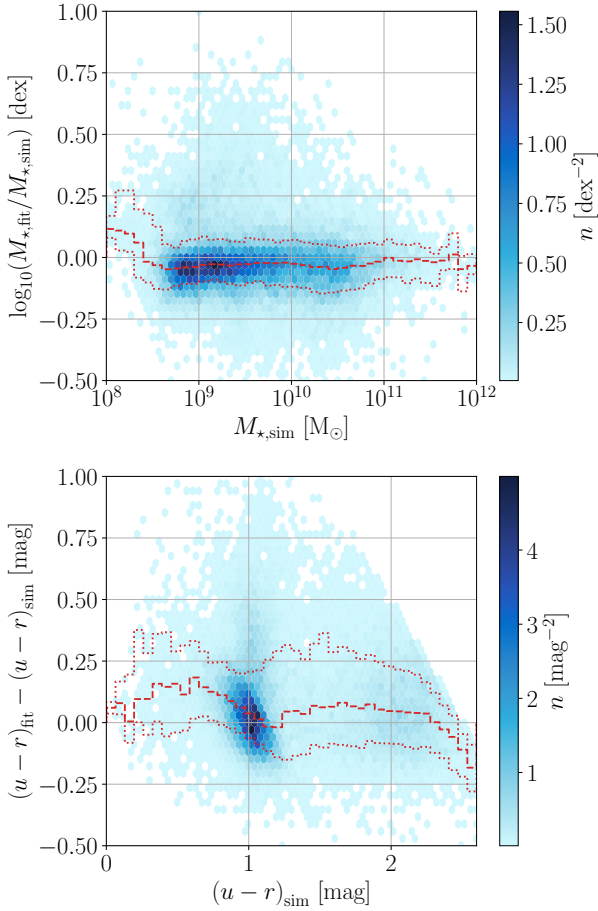


**Figure 1.** Comparison of the scatter between the fitted and intrinsic values to the intrinsic galaxy properties of SHARK. The upper panel shows this for the stellar masses and the lower panel for the rest-frame intrinsic colours. The colour of the bins represents their galaxy density, as shown by the colour bar. The dashed and dotted lines show the running medians and 16<sup>th</sup>-84<sup>th</sup> percentiles, respectively.

address this in more detail in Section 4, briefly, we find that the main consequence of this is an increased spread in both colour populations, particularly of the red sequence. While this complicates the interpretation of some of our results, these fits still provide valuable insight into the dependency of our results on our modelling choices.

### 3 MODELLING THE COLOUR EVOLUTION OF GALAXIES

The first step in studying galaxy colours is to define the colour we wish to explore. The results from Strateva et al. (2001) and Martin et al. (2007) lead to both NUV and  $u$  being common choices across the literature for the "blue" band, as they provide the best separation between the colour populations. As we are using intrinsic colours derived from either SED fitting or SAM generation, we are technically free to choose any band, as long as it is within the spectral range of the PROSPECT stellar templates. However, fitted SEDs depend on the quality of the photometry for each band, which

means that not all parts of the intrinsic SED will be equally reliable. (For GAMA, the UV photometry from GALEX has larger uncertainties compared to the optical photometry from VST, due to both fewer photon counts and larger point spread function. This translates to poorer fit constraints in NUV compared to  $u$ , and as such, we choose the latter as our "blue" band. We then pair this with  $r$  as our "red" band, generating colours in  $u - r$  (a choice shared with Strateva et al. 2001; Baldry et al. 2004; Schawinski et al. 2014; Trayford et al. 2016; Bremer et al. 2018; Wright et al. 2019). Our tests comparing specific star formation rates (sSFR) and  $u - r$  with all three samples show a narrow linear relation down to  $\sim 10^{-11} \text{ yr}^{-1}$  (though SHARK does exhibit more scatter), at which point  $u - r$  saturates.

At the core of this work then lies the choice of how to define a blue and red population in our  $u - r$  colour space. There is a wide variety of literature choices on how to separate these populations (e.g., Schawinski et al. 2014; T15; Trayford et al. 2016; Bremer et al. 2018; Wright et al. 2019), most of which are simple selection functions drawn by eye (i.e., defining a minimum colour for a galaxy to be blue). Since we will use our presented population model in future work to explore the colour transition timescales of galaxies (Bravo et al. in preparation), defining a single hard cut in colour (like in Bell et al. 2003; Baldry et al. 2004; Peng et al. 2010) to separate between blue and red populations is not appropriate. Such a classification is binary, with galaxies being either blue or red, with an effectively instantaneous transition timescale. The measurement of a timescale then requires a boundary region where galaxies are tagged as neither blue nor red. To overcome this, we devise a new method for tracking the blue and red populations over time, which can then be used to probabilistically assign galaxies to either population at a given epoch.

#### 3.1 Model overview

To study the colour evolution of galaxies from both GAMA and SHARK we use a method inspired by T15, who studied the observed  $z \sim 0$  colour population in GAMA. Briefly, their starting point was the assumption, corroborated in their analysis, that the colour distribution is well-represented by two Gaussians at any stellar mass. Then, they assumed that the means and standard deviations are a function of stellar mass, using a fairly flexible model (two smoothly-joined line segments). As their interest was in the stellar mass functions, they implicitly parameterised the weights of each Gaussian by assuming a double Schechter function (Schechter 1976) for each population. Finally, they also assumed a model to bias against poor data. In total, their model contains 40 free parameters. To obtain the best fitting values of these parameters they used a Markov chain Monte Carlo sampling to explore the parameter space, which for their sample of  $\sim 26,000$  galaxies required  $\sim 90,000$  CPU hours of computation.

We could simplify this model by ignoring both stellar mass function, which we do not intend to explore, and the bad data modelling. A simple two-parameter description for the weights, the minimum required to include a stellar mass dependency, would bring the number of free parameters down to 27. However, even with this simplification, using a simple linear model for the time evolution of each parameter would double this number and may not be enough to model the true measured colour evolution. This is exacerbated by our desire to also test fitting three populations instead of just two (to evaluate the existence of a third "green" population). Finally, T15 used a sample of 26,000 GAMA galaxies ( $z < 0.12$ ), while across our three samples we have 67,000 galaxies, times the 91 evolution-

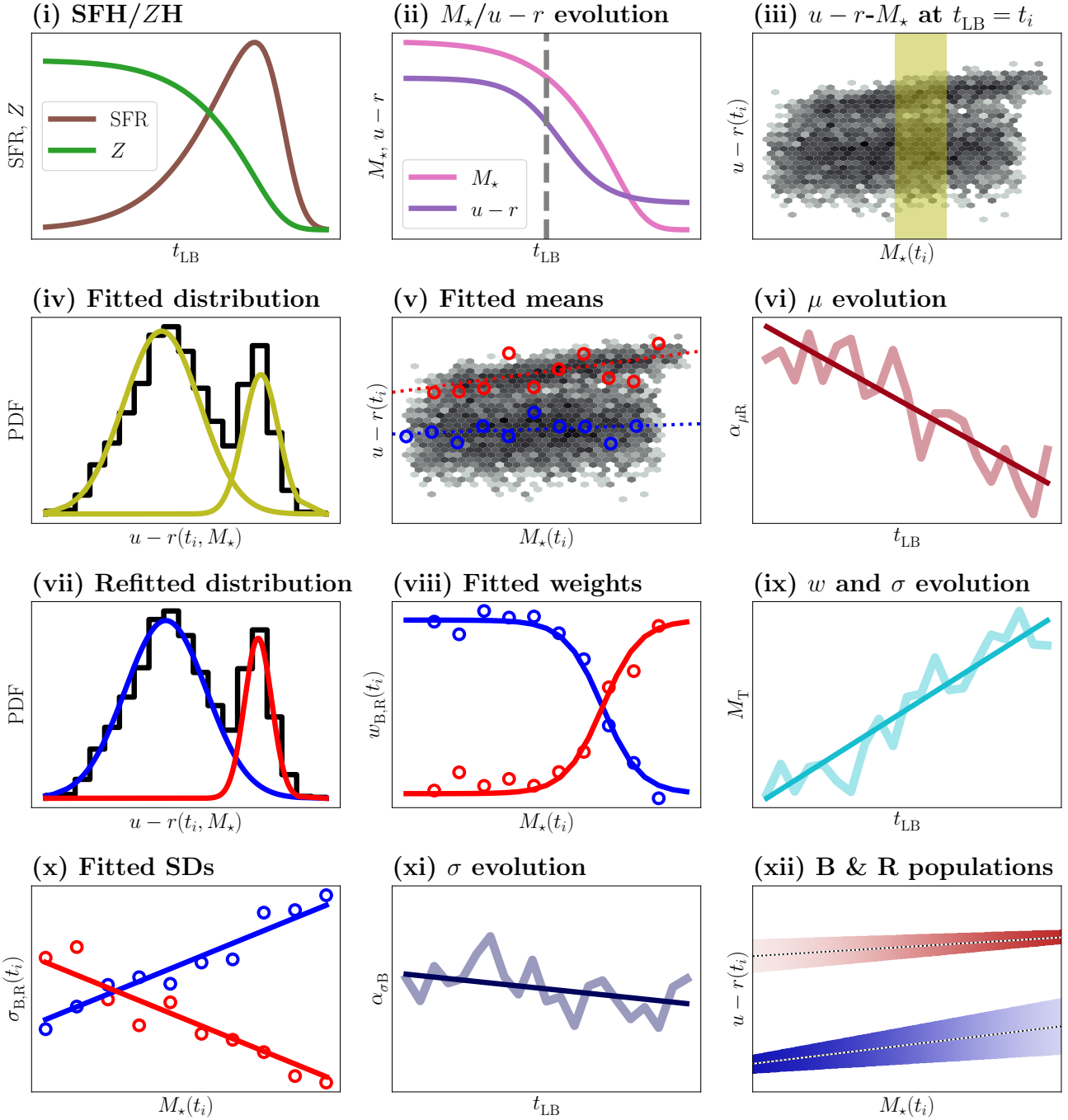


**Figure 2.** Schematic representation of the methodology employed in this work, using our two-component fit as an example. Our starting point (i, described in Section 2) are the SFHs and ZHs of the galaxies in each sample, retrieved either directly from SHARK (Section 2.2) or through SED fitting with ProSPECT (GAMA and SHARK<sub>fit</sub>, Sections 2.1 and 2.3). From those, we generate the stellar mass and colour histories for these galaxies (ii, Section 3.2), for every 100 Myr from 1 to 10 Gyr of lookback time, using the generative mode of ProSPECT. At each of these time steps, we bin the galaxies in stellar mass bins of a width 0.3 dex, and use a two- or three-component GMM to fit the colour distribution in each mass bin (iii and iv, Section 3.3). We then fit the blue and red populations with linear relations as a function of mass, and then we fit the slope and value at  $M_\star = 10^{10.5} M_\odot$  as a function of time (v and vi, Section 3.3.1). We show as an example a representation of the time evolution of the slope of the red means ( $\alpha_{\mu R}$ ). Next, we use these fits to fix the means of the components in our GMM and refit the populations (vii, Section 3.4). From these refits, we then first parameterise the dependency of the weights and standard deviations on stellar mass (viii and x, Section 3.4.1 for the weights and 3.4.2 for the standard deviations), followed by fits to the time evolution of these parameters (ix and xi, Sections 3.4.1 and 3.4.2). As example, we display a representation of the time evolution of two parameters: the mass where both populations have equal weights ( $M_T$ ), and the slope of the standard deviation as a function of stellar mass for the blue population ( $\alpha_{\mu B}$ ). With these parameterisations, we have a full description of the populations as a function of time (xii, Section 4), where the dotted lines show the means, the width show the standard deviations and the shading the weights.

ary time steps we use, giving a total of  $\sim 6, 100, 000$  implied data points. Due to these considerations, we opt against implementing the exact T15 method due to the large computational cost.

Instead, we choose to split our fitting into multiple simple steps. This greatly reduces computation time at the cost of requiring careful control of every step, to avoid fitting errors cascading throughout our method. Given the significant number of steps in our method, and the necessity to introduce 21 equations with 51 variables involved, here we provide a simple overview of this method, with the following subsections containing a detailed motivation and description of every step. Figure 2 also provides a visual representation of these steps.

(i) The foundation of this work are the SFHs and ZHs of the galaxies in our three samples: GAMA, SHARK and SHARK<sub>fit</sub>.

(ii) Given these SFHs and ZHs, we use ProSPECT to calculate the stellar mass and model the SED (to derive intrinsic colour) of each galaxy at a range of lookback times (from 1 to 10 Gyr, in 100 Myr steps).

(iii) At every time step we divide the galaxies in stellar mass bins with 0.3 dex width, chosen as the best balance between a robust measurement of the colour distribution for  $\log_{10}(M_{\star}/M_{\odot}) \in [9, 11]$  and a good number of bins sampling the red population.

(iv) We fit the colour distribution in each stellar mass bins using a two- or three-component Gaussian Mixture Model (GMM).

(v), (vi) We assign the Gaussians as being blue or red (or green for the three-component fit). We then fit the means, as a function of stellar mass, and parameterise the time evolution of these fits.

(vii) As the number of galaxies in each bin rapidly decays as one moves away from the median stellar mass, the fits do not show a smooth evolution between time steps (an expected outcome of individually fitting each mass bin). To obtain a smoother evolution for the standard deviations and weights we refit our GMM, this time fixing the means to values calculated with the evolution fit in the previous step.

(viii), (ix), (x), (xi) We fit the standard deviations and weights in the same manner as the means.

Panel (xii) of Figure 2 provides a schematic representation of the resulting parameterisation of the colour populations. The dotted lines indicate the means of each population, the widths show the standard deviations and the shading shows the weights. What follows for the remainder of this section is a detailed presentation of how we implement this method, together with the results from which we construct the representation of the colour evolution in our galaxy samples shown in Figure 11, the main summary of our results.

### 3.2 Converting SFH and ZH into $M_{\star}$ and $u - r$ histories

From the SFHs it is straightforward to generate stellar mass histories. In this work, we use the remaining stellar mass, not the formed stellar mass (i.e., removing the recycled stellar mass, see Robotham et al. 2020 for details). For SHARK, since recycling is instantaneous, this is calculated simply by integrating the SFH of the galaxy and scaling it by  $1 - f_{\text{recycled}}$ <sup>6</sup>. For GAMA and SHARK<sub>fit</sub> we calculate the remaining stellar mass with ProSPECT, which uses the lookup tables from the GALAXEV templates. For the colours, we use ProSPECT in its generative mode, in a similar manner to how we generated the

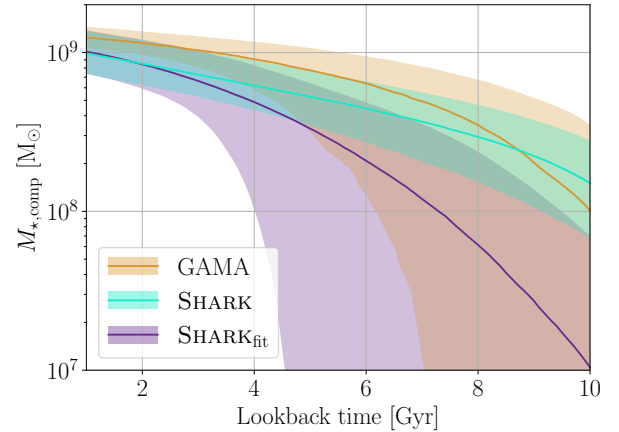


**Figure 3.** Evolution of the stellar masses of the galaxies 0.2 dex around the mass completeness of each sample. GAMA is shown in orange, SHARK in cyan and SHARK<sub>fit</sub> in purple. The solid lines show the median stellar mass at any given lookback time, with the shaded areas showing the 16<sup>th</sup>–84<sup>th</sup> percentile range.

synthetic SEDs described in Section 2.2, the big distinction being that we restrict the SFH and ZH to the lookback time of each time step. A movie showing the evolution in the colour- and specific star formation rate<sup>7</sup> (sSFR)-stellar mass planes of our three samples can be found in the supplemental material of this work.

While B20b selected the GAMA sample such that it is volume-limited, this does not ensure mass completeness. The challenge that reconstructing the evolution of this sample presents is how to model the evolution of the mass completeness. Since at any time step we have the same galaxies, we define mass completeness by tracking the galaxies around the mass completeness limit at observation time. The samples from GAMA and SHARK/SHARK<sub>fit</sub> differ slightly in their mass completeness, with the former having a higher completeness limit. We then select all galaxies in a 0.2 dex range around the mass completeness limit for each sample ( $9.0 < \log_{10}(M_{\star}/M_{\odot}) < 9.2$  for GAMA and  $8.9 < \log_{10}(M_{\star}/M_{\odot}) < 9.1$  for SHARK/SHARK<sub>fit</sub>), and trace their evolution with time.

We show the evolution of these galaxies in Figure 3. We find that SHARK and SHARK<sub>fit</sub> are in excellent agreement for lookback times below  $\sim 3$  Gyr, but start to diverge considerably by 4 Gyr. The divergence of the medians is not unexpected, given that we found a shallower evolution of the SFH in our ProSPECT fits to SHARK (i.e., a more gradual mass build-up). However, GAMA and SHARK<sub>fit</sub> are in remarkable agreement in the evolution of the dispersion, while dispersion is markedly smaller in SHARK, which shows that not all differences stem from the quality of our SED fits in SHARK<sub>fit</sub>. This points to the modelling choices we make (following B20b and Thorne et al. 2021), the parameterisation of the SFHs specifically, as the source of this increased scatter. As the medians are in reasonable agreement (when accounting for SFH differences) this is evidence that they are the more reliable tracer. For this reason, we use the medians to define the mass completeness for each sample as a function of time.

<sup>6</sup>  $f_{\text{recycled}} = 0.46$  for the Chabrier (2003) IMF used in SHARK, as described in section 4.4.6 of L18.

<sup>7</sup> Calculated by integrating the SFH for the previous 100 Myr to any given time step for all samples.

### 3.3 Unconstrained GMM and means parameterisation

We start with an unconstrained GMM fit to all stellar mass bins with at least 30 galaxies. These fits can be described by:

$$P_B(u-r) = \frac{1}{2\pi\sigma_B} \exp\left(-\frac{1}{2}\left(\frac{(u-r)-\mu_B}{\sigma_B}\right)^2\right) \quad (1)$$

$$P_R(u-r) = \frac{1}{2\pi\sigma_R} \exp\left(-\frac{1}{2}\left(\frac{(u-r)-\mu_R}{\sigma_R}\right)^2\right) \quad (2)$$

$$P(u-r) = w_B P_B(u-r) + w_R P_R(u-r) \quad (3)$$

where  $P(u-r)$  is the fitted PDF describing the colour distribution, composed by the weighted addition of the Gaussian distributions  $P_B(u-r)$  and  $P_R(u-r)$ , representing the blue and red populations. These are weighted by  $w_B$  and  $w_R$ , which are defined such that  $w_B + w_R = 1$ . The sets  $\{\mu_B, \sigma_B\}$  and  $\{\mu_R, \sigma_R\}$  are the means and standard deviations of  $P_B(u-r)$  and  $P_R(u-r)$ , respectively. In this step, the set of free parameters is then  $\{w_B, \mu_B, \sigma_B, w_R, \mu_R, \sigma_R\}$ . It is worth noting that, in the definitions presented, for a cleaner notation we have ignored the fact that all of these quantities are a function of both stellar mass and lookback time, but we fit them at each stellar mass bin and time step.

We also tested an equivalent three-component model:

$$P(u-r) = w_B P_B(u-r) + w_x P_x(u-r) + w_R P_R(u-r)$$

where  $P_x(u-r)$  follows the same equation as  $P_B(u-r)$  and  $P_R(u-r)$ . We found that, like T15, two was sufficient, with small weights ( $w_x < 0.1$ ) and large standard deviations ( $\sigma_x \gtrsim 1$  mag) fitted for the third component. Furthermore, the model consistently used the added flexibility of this third component to fit features outside the space between blue and red populations (hence the use of  $x$  subscripts instead of  $G$ ). For this reason, we will only present and discuss results for the two-component GMM fits.

The left column of Figure 4 shows three examples of these fits for GAMA. For the bluer component, the slope as a function of stellar mass ( $\alpha_{\mu_B}$ ) increases at lower lookback times, which is driven by the high-mass end becoming redder, while near the mass completeness limit the locus remains nearly constant. By contrast, the redder components (not merged with the bluer) show a weaker evolution, showing a shallower slope at recent times, driven by the reddening of the low-mass end. Near the completeness limit, both components show significant overlap, though it is clear that the redder Gaussian is becoming redder with time.

To parameterise the means of both populations, we first need to choose which stellar mass bins and GMM components to use. Firstly, to remove poor fits we discard all fits for which the reduced chi-square ( $\chi^2_{\nu}$ ) is outside the range  $[0.85, 1.1]$ <sup>8</sup>, which removes a median of one mass bin per time step. At this point, we have the second significant difference between our approach and that of T15, as we consider the existence of a red population only when there is a local minimum in the combined PDF between the means of

both Gaussians. Where this is not the case we consider the dominant component as tracing the blue population, with the secondary accounting for non-Gaussianities. We further impose a limit in both the minimum separation of the means (not smaller than 0.5 mag) and the maximum standard deviations (not greater than 0.3 mag), to ensure a clean selection for both populations. These shared selection criteria are then:

$$\left(\chi^2_{\nu} \in [0.95, 1.1]\right) \wedge (\mu_R - \mu_B > 0.5) \wedge (\sigma_{\{B,R\}} < 0.3).$$

Finally, to remove the fits at very high masses, which have a small number of galaxies ( $\lesssim 0.5\%$  of the full sample), we consider only means from fits below  $10^{10.5}$  and  $10^{11} M_{\odot}$  for the blue and red populations, respectively. The result from this selection is shown in Figure 5 with open (removed) and solid (included) markers.

Before we detail how we parameterise the means ( $\mu_{\{B,R\}}$ ), weights ( $w_{\{B,R\}}$ ) and standard deviations ( $\sigma_{\{B,R\}}$ ) of the GMM fits (Sections 3.3.1, 3.4.1 and 3.4.1, respectively), we discuss two aspects here. For the fits, we choose the function with the fewest free parameters, to ensure both a good representation of the data and a stable parameter evolution with time. Furthermore, we first parameterise the means of the components from the GMM fit, and then those parameterisations as a function of time.

As such, it is worth describing the nomenclature convention we adopt for the different parameters. For the parameterisation as a function of stellar mass, we use first-order polynomials for the means and standard deviations, where  $\alpha$  indicates the first-order term and  $\beta$  the zeroth-order. As an example,  $\alpha_{\mu_B}$  then represents the slope as a function of stellar mass of the means of the blue population ( $\mu_B$ ). The parameterisation of the weights as a function of stellar mass does not follow this convention, as we use a noticeably different parameterisation, for which the parameters have a different physical interpretation. For the temporal parameterisation, we use a numbered subscript to indicate the order, though note that it is not necessarily indicative of a polynomial expression, as we use a greater variety of functional forms for these fits. I.e.,  $\alpha_{0\mu_B}$  is the zeroth order of the time evolution of the slope as a function of stellar mass ( $\alpha_{\mu_B}$ ) of the mean of the blue population ( $\mu_B$ ).

#### 3.3.1 Means parameterisation

We use the following equations to fit the means as a function of stellar mass for both populations, at every time step:

$$\mu_B = \alpha_{\mu_B} \log_{10}(M_{\star}/10^{10.5} M_{\odot}) + \beta_{\mu_B} \quad (4)$$

$$\mu_R = \alpha_{\mu_R} \log_{10}(M_{\star}/10^{10.5} M_{\odot}) + \beta_{\mu_R} \quad (5)$$

where  $\{\alpha_{\mu_B}, \alpha_{\mu_R}\}$  are the slope of the means as a function of stellar mass, and  $\{\beta_{\mu_B}, \beta_{\mu_R}\}$  are the value of the means at a stellar mass of  $10^{10.5} M_{\odot}$ <sup>9</sup>. Figure 5 shows that, given our choices to select points as accurately representing either population, these parameterisations provide a good representation of the data.

<sup>8</sup> Our choice of this non-symmetric range comes from a detailed inspection of the GMM [unconstrained] fits. Fits with  $\chi^2_{\nu}$  values of 0.85-0.90 tend to properly capture the red population at low stellar masses, while those in the 1.10-1.15 range are driven by one of the two components being a poor fit, leaving a significant part of the true distribution unaccounted for. We remark that, as stated before, this is not evidence of a third ("green") population, as a third component does not improve these fits. Instead, this is a consequence of our approach of fitting each time step and mass bin individually, which leads to poorer fits where one of the populations is strongly dominant.

<sup>9</sup> There is nothing particularly meaningful about this choice of stellar mass. The main reasons for this choice are that 1) the intercepts with the y-axis ( $\log(M_{\star}/M_{\odot}) = 0$ ) can be dominated by small fluctuations in  $\{\alpha_{\mu_B}, \alpha_{\mu_R}\}$ , and 2) this particular stellar mass is a commonly quoted value for the well-known  $M^*$  at  $z = 0$  (the "knee" of the stellar mass function).



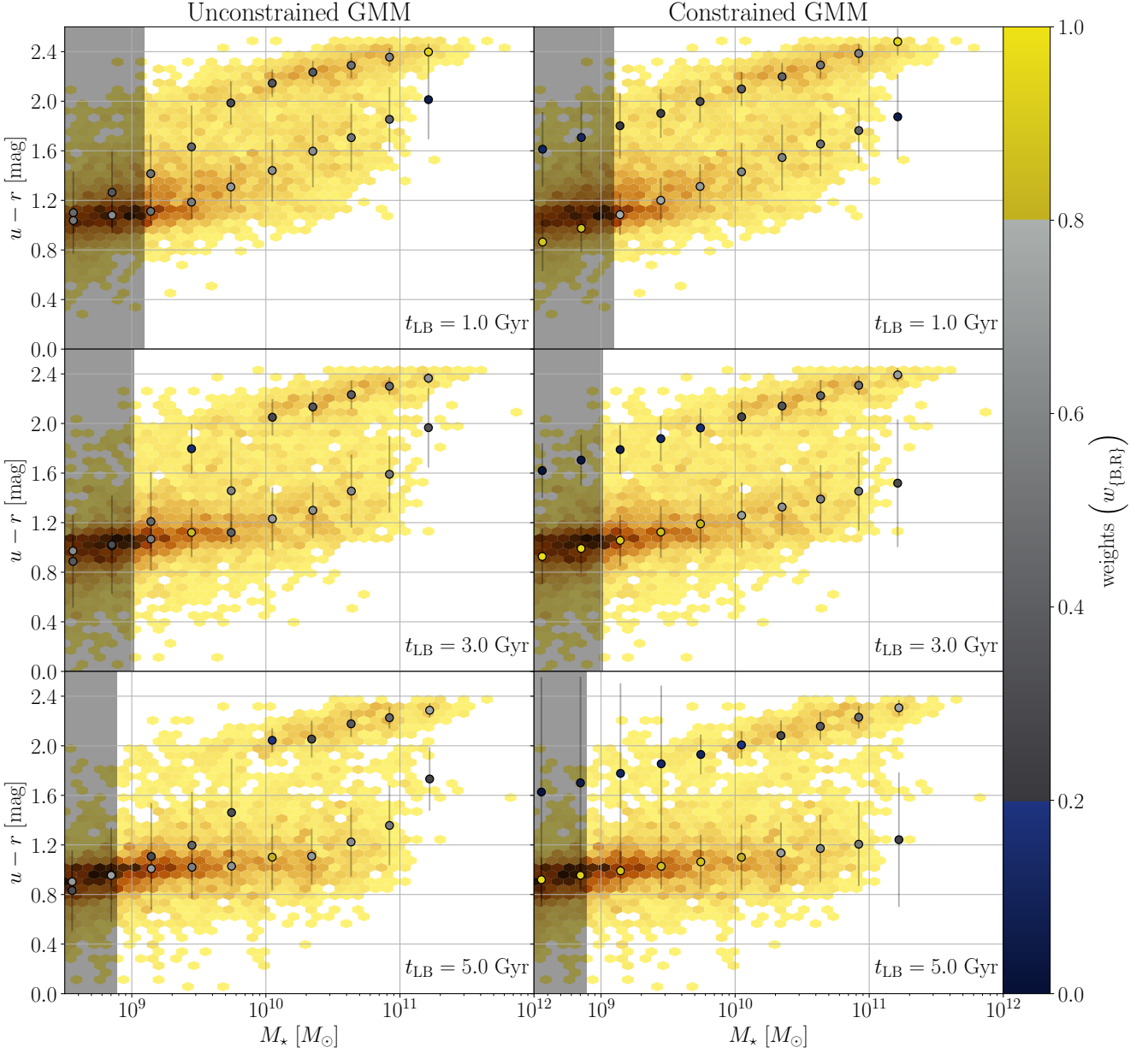


**Figure 4.** Example of the results from the unconstrained (left column) and constrained (right column) GMM fits to GAMA data at three time steps (1, 3 and 5 Gyr, from top to bottom). Each panel shows the distribution of rest-frame intrinsic  $u-r$  colours and stellar mass, together with a display of the resulting fits from the GMM. Histogram bins show the 2D PDF, with colour range optimised for each panel to display the relative distribution of galaxies. The position of the markers shows the mean ( $\mu_{\{B,R\}}$ ) of each Gaussian component. The inner colour of the markers shows the weights ( $w_{\{B,R\}}$ ), following the colour bar shown on the right. The vertical bars show the standard deviation ( $\sigma_{\{B,R\}}$ ). The grey shaded regions show the stellar masses below the mass completeness limit.

To fit the time evolution of these parameters we use the following set of equations:

$$\alpha_{\mu B} = \alpha_{2\mu B} t_{LB}^2 + \alpha_{1\mu B} t_{LB} + \alpha_{0\mu B} \quad (6)$$

$$\beta_{\mu B} = \beta_{2\mu B} t_{LB}^2 + \beta_{1\mu B} t_{LB} + \beta_{0\mu B} \quad (7)$$

$$\alpha_{\mu R} = \alpha_{1\mu R} t_{LB} + \alpha_{0\mu R} \quad (8)$$

$$\beta_{\mu R} = \beta_{1\mu R} t_{LB} + \beta_{0\mu R} \quad (9)$$

where  $\alpha_{\mu B}$  and  $\beta_{\mu B}$  are fit with second-order polynomials as a function of lookback time ( $t_{LB}$ ), of free parameters  $\{\alpha_{2\mu B}, \alpha_{1\mu B}, \alpha_{0\mu B}\}$

and  $\{\beta_{2\mu B}, \beta_{1\mu B}, \beta_{0\mu B}\}$ , and  $\alpha_{\mu R}$  and  $\beta_{\mu R}$  are fit with first-order polynomials, of free parameters  $\{\alpha_{1\mu R}, \alpha_{0\mu R}\}$  and  $\{\beta_{1\mu R}, \beta_{0\mu R}\}$ .

Figure 6 shows the results from these fits. Starting with the blue population, the assumed models within ProSPECT are apparent again in the evolution of the slope, as while both SHARK and SHARK<sub>fit</sub> show the matching slopes at low lookback times, the same is not true above  $\sim 5$  Gyr, where SHARK<sub>fit</sub> is well-matched with GAMA. From this, we can conclude that the blue population in SHARK is too shallow compared to observations at low lookback times, but no firm conclusion can be drawn at older times as our SED fitting does

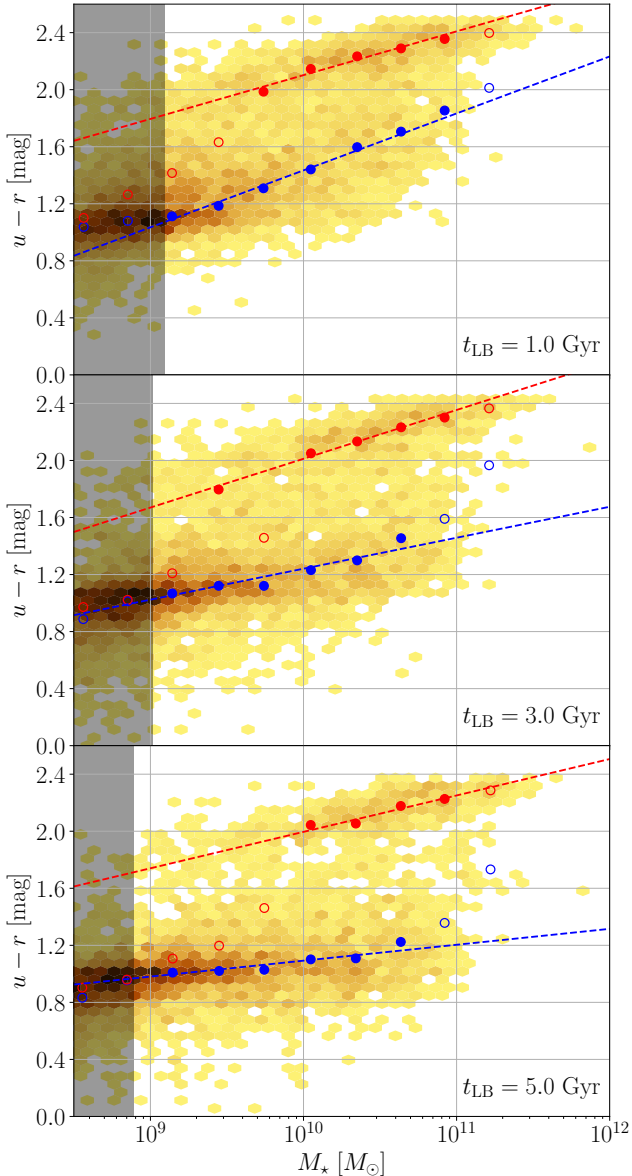


**Figure 5.** Example of the parameterisation of the means ( $\{\mu_B, \mu_R\}$ ) of the Gaussian components, as a function of stellar mass. Panels and histograms as in the left column of Figure 4. The blue and red points show the selected means assigned to either the blue or red population, respectively. The blue and red curves show the fitted parameterisation to each, defined by Equations 4 and 5. Open markers denote the points not used to fit the curves. Histograms and shaded regions as in Figure 4.

not recover the true evolution (Appendix A). This is not the case for the value of the means at  $M_\star = 10^{10.5} M_\odot$ , where both SHARK and SHARK<sub>fit</sub> are in good agreement at all times, meaning that the evolution measured for GAMA is not informed by ProSPECT. This points to another discrepancy between SHARK and GAMA which, combined with the difference in slopes, translates to SHARK galaxies at 1 Gyr being bluer than GAMA for  $M_\star \gtrsim 10^8 M_\odot$ .

The red population becomes well established in GAMA  $\sim 3$  Gyr earlier than in SHARK/SHARK<sub>fit</sub> which is driven by the earlier appearance of a significant population of red galaxies below a stellar mass of  $\sim 10^{10} M_\odot$ . The evolution of the slopes suggests that

ProSPECT may be biasing the recovered evolution by shifting the population, unlike forcing it to a certain path like the blue population at high lookback times, though we caution that this could be an effect of the fit quality in SHARK<sub>fit</sub>. Finally, while the difference in  $\mu_R$  at  $M_\star = 10^{10.5} M_\odot$  ( $\beta_{\mu_R}$ ) between SHARK and SHARK<sub>fit</sub> is systematic, the offset is small ( $\lesssim 0.1$  mag). This is smaller than the difference between SHARK/SHARK<sub>fit</sub> to GAMA, suggesting any potential systematic effect introduced by ProSPECT cannot account for the difference between simulations and observations.

### 3.4 Constrained GMM and standard deviation/weights parameterisation

With  $\mu_{(B,R)}$  fully parameterised, we then repeat the GMM fits using these parameterisations to fix the means. The right column of Figure 4 displays the results of this refit, which in comparison with the left column shows that our parameterisation is well behaved. Not shown in the Figure is that this refit does affect the fits in a statistical sense, as the  $\chi^2_\nu$  values increase in spread (from  $\sim 0.9$ - $1.1$  to  $\sim 0.8$ - $1.2$ ), with the values now showing a clear trend in stellar mass (higher  $\chi^2_\nu$  with higher  $M_\star$ ). This trend should not come as a surprise, as it is clear that the red population has greatly decreased contribution to the overall population at low masses, so by forcing only one of the Gaussians to account for most of the population (as seen by comparing the weights between columns) a smaller value is expected. At higher masses, our assumption of linearity is not ideal, as small offsets can be seen in the means between columns, which leads to our refits to account for most, but not all, of the colour distribution. We remark that this change is small, so this does not provide a strong argument against this parameterisation of the weights. Furthermore, our definition of blue and red is not purely phenomenological, as we are not asking which two Gaussian components best describe the colour distribution, but which two "distinct" components do.

From Figure 4 it can be seen that, as with the means, not all fits provide meaningful information. As an example, the weights and standard deviations of the red components below  $\sim 10^{9.5} M_\odot$  in the bottom-right panel indicate that they are being used to fit a small residual population from the main (blue) population, with no identifiable red population. As with the means, we make several selection cuts. We retain the same selection criteria of distinguishable populations (local minimum present between means), quality of fit ( $\chi^2_\nu$ ) and maximum stellar mass as before, only mildly increasing the maximum standard deviation allowed to 0.4 mag.

#### 3.4.1 Weights parameterisation

From these fits we first proceed to parameterise the weights ( $\{w_B, w_R\}$ ) and standard deviations ( $\{\sigma_B, \sigma_R\}$ ) of the distributions. For the weights, we first fit them with logistic curves as a function of stellar mass:

$$w_R = \{1 + \exp[-k(\log_{10}(M_\star) - M_T)]\}^{-1} \quad (10)$$

$$w_B = 1 - w_R \quad (11)$$

where  $M_T$  is the stellar mass where both populations have equal weights and  $k$  defines the sharpness of the transition<sup>10</sup>. This parameterisation naturally models two populations where one dominates above  $M_T$  and the other below, with the benefit of only requiring

<sup>10</sup> The slope of the curve at  $M_T$  is one quarter of  $k$ ,  $w'_R(M^T) = k/4$ .

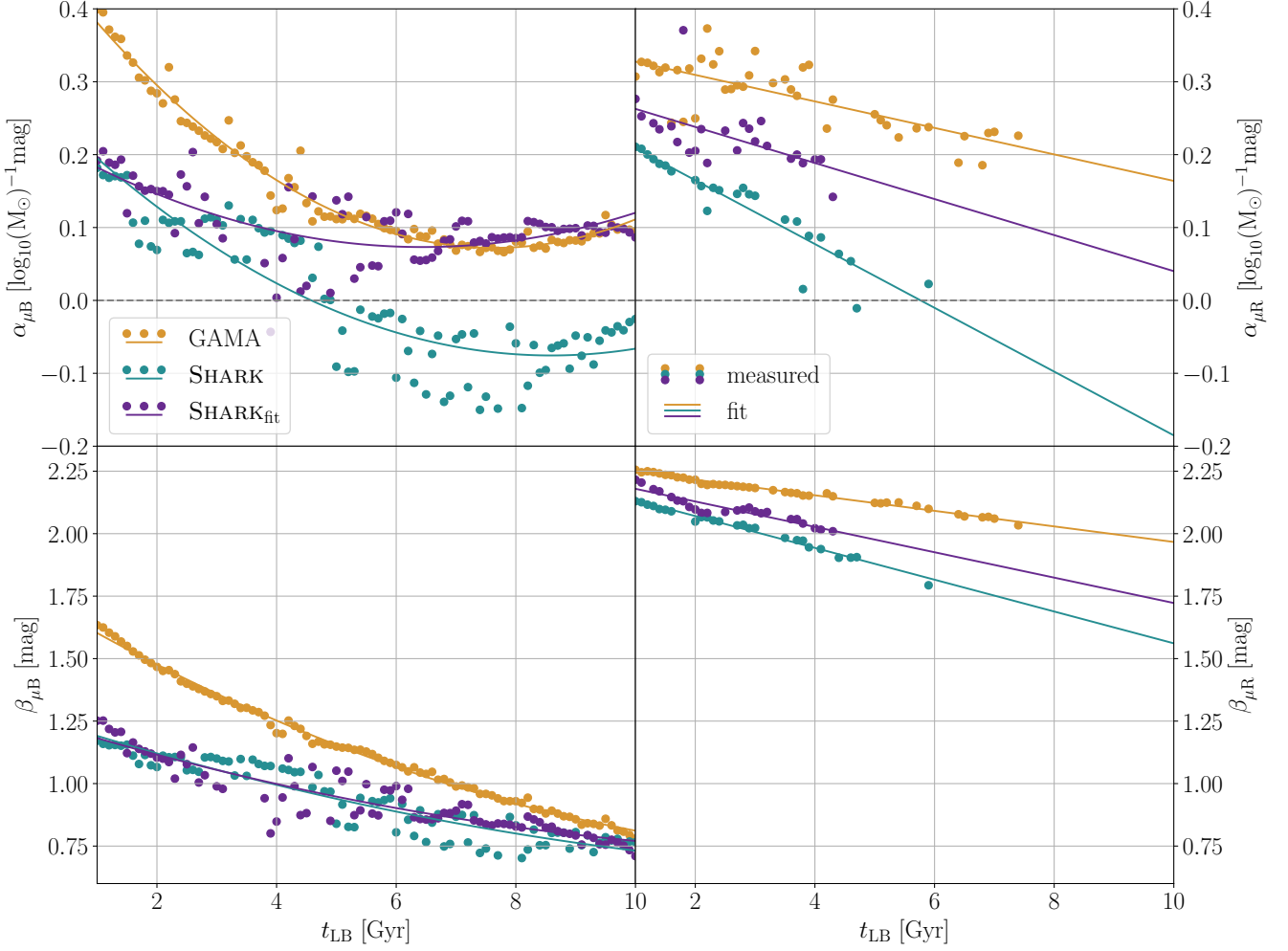


**Figure 6.** Time evolution of the blue and red population mean parameterisations. Colours as in Figure 3. The left column shows the results for the blue population and the right for the red population. In the top row, the evolution of the slope of the means as a function of stellar mass ( $\alpha_{\mu B}$ ,  $\alpha_{\mu R}$ , Equations 4 and 5) is shown with the round markers, and the fit to these (Equations 6 and 8) with solid lines. The bottom shows the value of the means at  $M_{\star} = 10^{10.5} M_{\odot}$  ( $\beta_{\mu B}$ ,  $\beta_{\mu R}$ , Equations 4 and 5) and fits (Equations 7 and 9) in the same manner.

two free parameters for a description of both. Figure 7 shows three examples of these fits for GAMA, which shows that this model is well justified by the data, even for points that have not been used to fit the free parameters.

Figure 8 shows that, unlike the rest of this work, we require different parameterisations for the time evolution of the weights for GAMA and SHARK/SHARK\_fit. For  $M_T$  we find that the evolution in GAMA is well-fitted by the second-order polynomial:

$$M_T = M_{2T} t_{LB}^2 + M_{1T} t_{LB} + M_{0T} \quad (12)$$

where  $\{M_{2T}, M_{1T}, M_{0T}\}$  are the free parameters. While this parameterisation produces a reasonable fit for SHARK and SHARK\_fit, we found that the following exponential representation improves the fit without increasing the number of free parameters:

$$M_T = \exp(M_{2T} t_{LB} + M_{1T}) + M_{0T} \quad (13)$$

The difference is more stark for  $k$ , where GAMA can be fitted by just a linear relation:

$$k = k_1 t_{LB} + k_0 \quad (14)$$

where  $\{k_1, k_0\}$  are the free parameters, but SHARK and SHARK\_fit require a second-order polynomial:

$$k = k_2 t_{LB}^2 + k_1 t_{LB} + k_0 \quad (15)$$

where  $\{k_2, k_1, k_0\}$  are the free parameters.

This is evidence that PROSPECT does not overtly influence the evolution of the weights. The difference between SHARK and SHARK\_fit is a result of the slower mass build-up in our fits, with galaxies becoming red at a slower rate leading to a softer transition between both populations and a higher transition mass. By  $t_{LB} = 6.0$  Gyr this reaches the point where the weights of both blue and red populations show no evolution with stellar mass, which is the driver for the diverging nature of  $M_T$  in SHARK\_fit. Interestingly, that we find  $M_T$  in SHARK to be lower than in GAMA for most lookback times (by  $\sim 0.2$  dex at  $t_{LB} = 1.0$  Gyr), as with a more qualitative assessment in Bravo et al. (2020) we found that in dust-attenuated  $g-i$  the opposite to be true (SHARK transitioning  $\sim 0.3$  dex higher). While there are caveats in this comparison, mainly that here we use a subset of one simulation and intrinsic  $u-r$  colour instead of

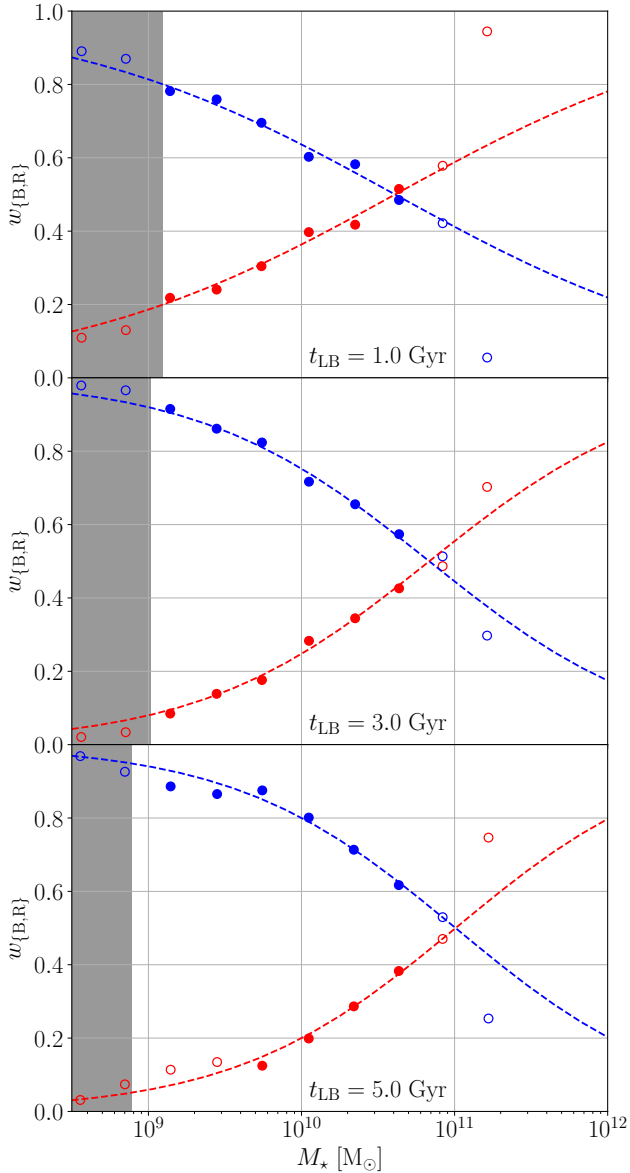


**Figure 7.** Example of the parameterisation of the weights  $\{w_B, w_R\}$  of the Gaussian components, as a function of stellar mass. Lookback times, shaded areas and points and curve colours as in Figure 5. Curves defined by Equations 10 and 11.

the GAMA lightcone and attenuated  $g-i$  of Bravo et al. (2020)<sup>11</sup>, this suggests that the driver of this difference is our dust model in SHARK.

### 3.4.2 Standard deviations parameterisation

Katsianis et al. (2019); Davies et al. (2019a, in preparation) found

<sup>11</sup> Our use of absolute magnitude and apparent magnitudes in Bravo et al. (2020) is a secondary concern, as in both cases we are dealing with low redshifts, which are also roughly comparable,  $z = 0.0668$  compared to  $0.003 < z < 0.12$  in Bravo et al. (2020).

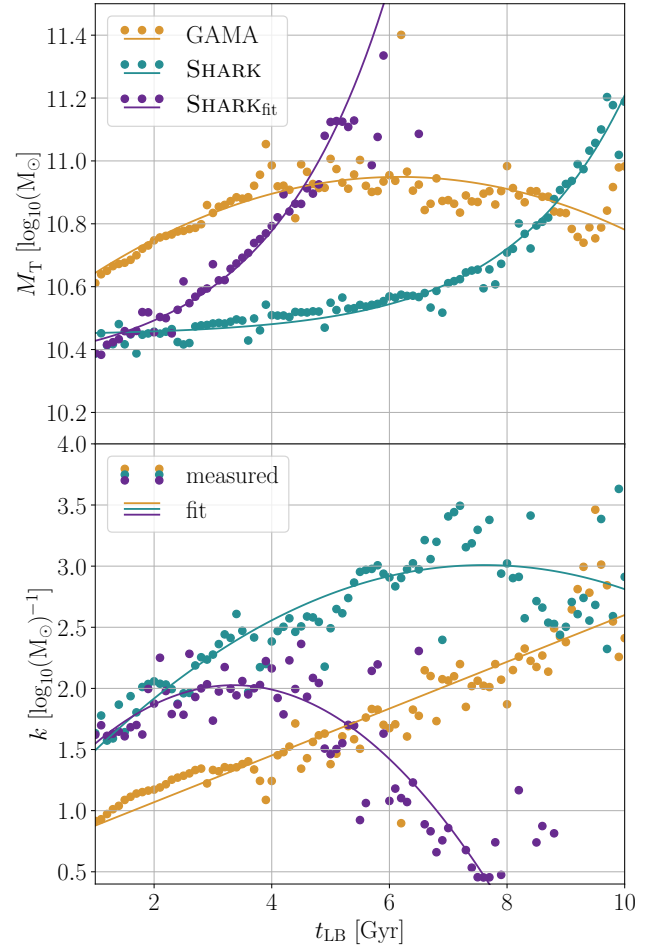


**Figure 8.** Time evolution of the blue/red population weights parameterisation. Curves and markers as in Figure 6. The top panel shows the evolution of the transition mass ( $M_T$ , Equation 10) and fits (Equations 12 and 13). The bottom shows the evolution of the sharpness of the transition ( $k$ , Equation 10) and fits (Equations 14 and 15) in the same manner.

that the galaxy star-forming main sequence displays a local minimum dispersion at  $\sim 10^9 M_\odot$ , which can be well described by a second-order polynomial. We considered a similar choice for the parameterisation of the standard deviation of the blue population, but we find no evidence of a similar behaviour above our chosen mass limit, as shown in Figure 9.

For this reason, we have fitted both standard deviations using linear relations as a function of mass:

$$\sigma_B = \alpha_{\sigma_B} \log_{10}(M_\star/10^{10.5} M_\odot) + \beta_{\sigma_B} \quad (16)$$

$$\sigma_R = \alpha_{\sigma_R} \log_{10}(M_\star/10^{10.5} M_\odot) + \beta_{\sigma_R} \quad (17)$$

where  $\{\alpha_{\sigma_B}, \alpha_{\sigma_R}\}$  are the slopes of the relation and  $\{\beta_{\sigma_B}, \beta_{\sigma_R}\}$  the values of the standard deviations at  $M_\star = 10^{10.5} M_\odot$ . One limitation of this approach, as seen in Figure 9, is that we run the risk of under-predicting the standard deviations at either stellar mass end. Examining all three samples we find that sensible lower limits are 0.12 and 0.08 mag for the blue and red populations respectively. This is effectively adding a third free parameter to our model, being equivalent in degrees of freedom as a second-order fit, but better capturing the observed distribution of the standard deviations.

For the time evolution we found that second-order polynomials



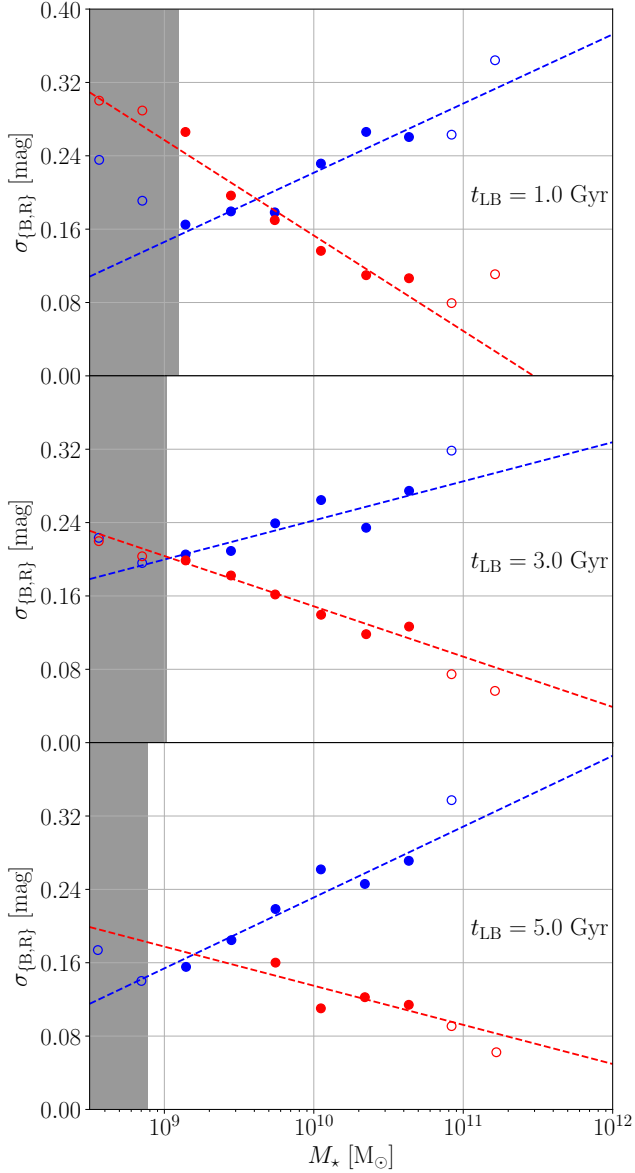


**Figure 9.** Example of the parameterisation of the standard deviations ( $\{\sigma_B, \sigma_R\}$ ) of the Gaussian components, as a function of stellar mass. Lookback times, shaded areas and points and curve colours as in Figure 5. Curves defined by Equations 16 and 17.

provide a good description for all parameters:

$$\alpha_{\sigma_B} = \alpha_{2\sigma_B} t_{LB}^2 + \alpha_{1\sigma_B} t_{LB} + \alpha_{0\sigma_B} \quad (18)$$

$$\beta_{\sigma_B} = \beta_{2\sigma_B} t_{LB}^2 + \beta_{1\sigma_B} t_{LB} + \beta_{0\sigma_B} \quad (19)$$

$$\alpha_{\sigma_R} = \alpha_{2\sigma_R} t_{LB}^2 + \alpha_{1\sigma_R} t_{LB} + \alpha_{0\sigma_R} \quad (20)$$

$$\beta_{\sigma_R} = \beta_{2\sigma_R} t_{LB}^2 + \beta_{1\sigma_R} t_{LB} + \beta_{0\sigma_R} \quad (21)$$

with  $\{\alpha_{2\sigma_B}, \alpha_{1\sigma_B}, \alpha_{0\sigma_B}\}$ ,  $\{\beta_{2\sigma_B}, \beta_{1\sigma_B}, \beta_{0\sigma_B}\}$ ,  $\{\alpha_{2\sigma_R}, \alpha_{1\sigma_R}, \alpha_{0\sigma_R}\}$  and  $\{\beta_{2\sigma_R}, \beta_{1\sigma_R}, \beta_{0\sigma_R}\}$  being the free parameters of each equation, respectively. Figure 10 shows the evolution of the standard deviation and our fits.

The similar slopes of the blue standard deviation between GAMA and SHARK<sub>fit</sub> suggest that this is another aspect of the colour

evolution that is informed by the modelling choices in ProSPECT, particularly given that SHARK is noticeably different from both. The value of the dispersion at  $M_* = 10^{10.5} M_\odot$  is another point where the quality of the fits in SHARK<sub>fit</sub> affects our results, as a slower mass build-up naturally leads to broader distributions. Still, the difference in slopes but agreement in values at  $10^{10.5} M_\odot$  between GAMA and SHARK implies that the variety of SFH/ZH that ProSPECT allows is greater than what is produced by SHARK (this is also seen in Figure 3). So while the agreement between GAMA and SHARK is remarkable, it is not possible to confirm if this means that SHARK reproduces well the observed dispersion at  $M_* = 10^{10.5} M_\odot$ .

The slope of the red dispersion shows several interesting features. Starting with GAMA and SHARK, it is interesting that they display slopes of opposite sign, with dispersion becoming smaller at higher and lower stellar masses, respectively. While likely affected by the quality of our fits, that SHARK<sub>fit</sub> is in better agreement with SHARK than GAMA shows that the difference between these last two is not purely attributable to ProSPECT. Similar but clearer is the evolution of the standard deviation of the red population at  $M_* = 10^{10.5} M_\odot$ , where both SHARK and SHARK<sub>fit</sub> are closer to each other than to GAMA. The latter displays a significantly smaller dispersion.

## 4 DISCUSSION

With the results presented in the previous section, we are in a position to provide potential answers to the questions we formulated in Section 1 (see Section 4.1). Given certain assumptions, we can also predict the future colour evolution of galaxies (see Section 4.2).

### 4.1 Reconstructing past galaxy colour evolution

As mentioned in Section 1, before we can address the main question (i), there are three related questions (ii-iv) we must first consider. To answer these, Figure 11 presents a schematic view of the evolution of both blue and red populations for our samples, together with maps showing the probability of being red for each of the schematic panels.

#### 4.1.1 (ii) How well we can reconstruct the colour evolution of galaxies from their panchromatic SEDs?

To fully assess our fitting method we need to compare the results from applying our reconstruction methodology to our simulations (SHARK<sub>fit</sub>) to the intrinsic predictions. We can describe the galaxy population in SHARK using the same parameterisations as GAMA (besides the time evolution of the weights), given that in Bravo et al. (2020) we showed that there is a good agreement in the colour distribution at low redshift between GAMA and SHARK. We also find that the same functional forms successfully describe the colour evolution in both SHARK and SHARK<sub>fit</sub>. This implies that any effect from SED fitting with ProSPECT will be at most on the quantitative values of the parameterisation.

Comparing GAMA and SHARK, the blue and red populations occupy broadly the same region in the colour-stellar mass plane and evolve similarly. One key difference is that the means of both colour populations show a weaker dependence on stellar mass in SHARK than in GAMA at all epochs. Since  $u-r$  is strongly correlated to sSFR and metallicity (both gas and stellar), this suggests that either both populations show less of a dependence on stellar mass

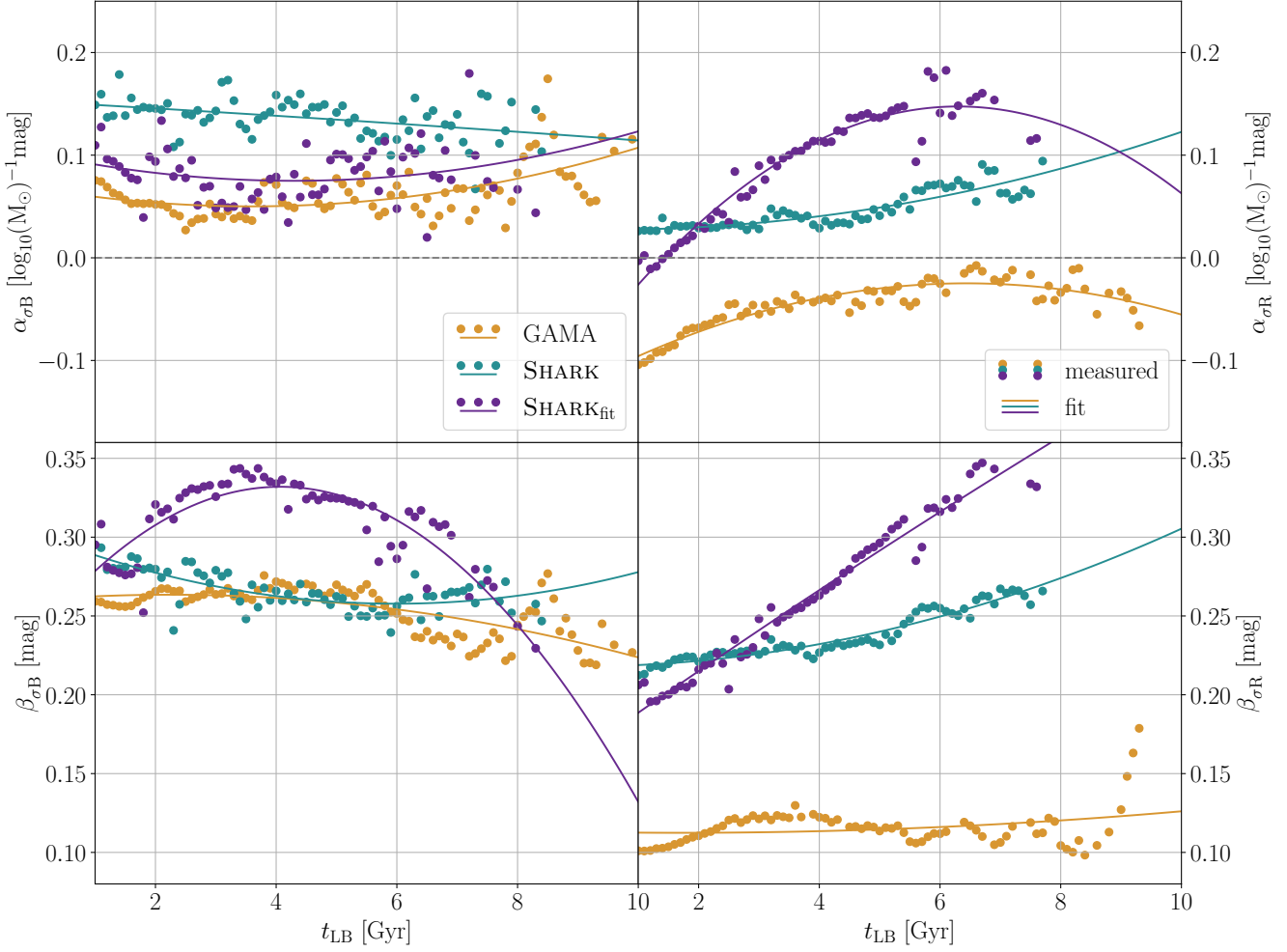


**Figure 10.** Time evolution of the blue and red population standard deviation parameterisations. Curves and markers as in Figure 6. The left column shows the results for the blue population and the right for the red population. In the top row, the evolution of the slope of the standard deviation as a function of stellar mass ( $\{\alpha_{\sigma B}, \alpha_{\sigma R}\}$ , Equations 16 and 17) is shown with the round markers, and the fit to these (Equations 18 and 20) with solid lines. The bottom shows the value of the standard deviations at  $M_\star = 10^{10.5} M_\odot$  ( $\{\beta_{\sigma B}, \beta_{\sigma R}\}$ , Equations 16 and 17) and fits (Equations 19 and 21) in the same manner.

in SHARK, or that the dependence is such that they mostly balance each other out.

Another difference is the width of the red population at the high-mass end, where SHARK exhibits the opposite trend to GAMA: massive red galaxies are more varied in colour, compared to the low-mass end of the red population. From a detailed analysis of the colour distribution of massive galaxies ( $M_\star > 10^{10.5} M_\odot$ ) in SHARK, we find evidence suggesting that the blue population might not be symmetric (i.e., non-Gaussian), being biased toward redder colours. This would not be enough to bring SHARK into agreement with GAMA. This, combined with the better agreement between SHARK and SHARK\_fit (in the values of  $\beta_{\sigma R}$  in Figure 10), indicates that the stellar populations of red massive galaxies are intrinsically more varied in SHARK than in GAMA. Since  $u-r$  becomes insensitive to sSFR below  $\lesssim 10^{-11}$  Gyr, this points to an excessive variation in stellar metallicities for these galaxies in SHARK.

The effect of these differences can be seen in the maps showing the probability of being red ( $P_R$ ) in Figure 11, where SHARK shows a transition region larger than GAMA by a factor of  $\sim 4$  at the high-

mass end. We will explore how this affects the colour transition timescales of massive galaxies in our next paper.

The comparison between SHARK\_fit and SHARK shows that there are some differences between GAMA and SHARK that are driven by systematic effects of our reconstruction technique. Some of these differences are driven by the quality of our SED fits to SHARK. Some poor fits are due to a sub-optimal choice of errors/priors, while others derive from SHARK galaxies becoming metal-rich significantly earlier than allowed by ProSPECT (see Appendix A). Both issues lead to a reconstructed SFH from SHARK\_fit that is flatter than the one predicted by SHARK. We will now discuss the tensions between SHARK and SHARK\_fit that are not attributable to the aforementioned two issues.

At early times SHARK displays a negative slope with stellar mass (more massive galaxies are bluer), which is not seen in SHARK\_fit (nor in GAMA). This indicates that we are not able to recover the true slope of the populations at early times ( $\gtrsim 6$  Gyr) using ProSPECT, i.e., the skewed normal SFHs we use in ProSPECT force massive galaxies to be less star-forming than they may be in reality. Lower mass galaxies are in general better recovered. As old stars have a

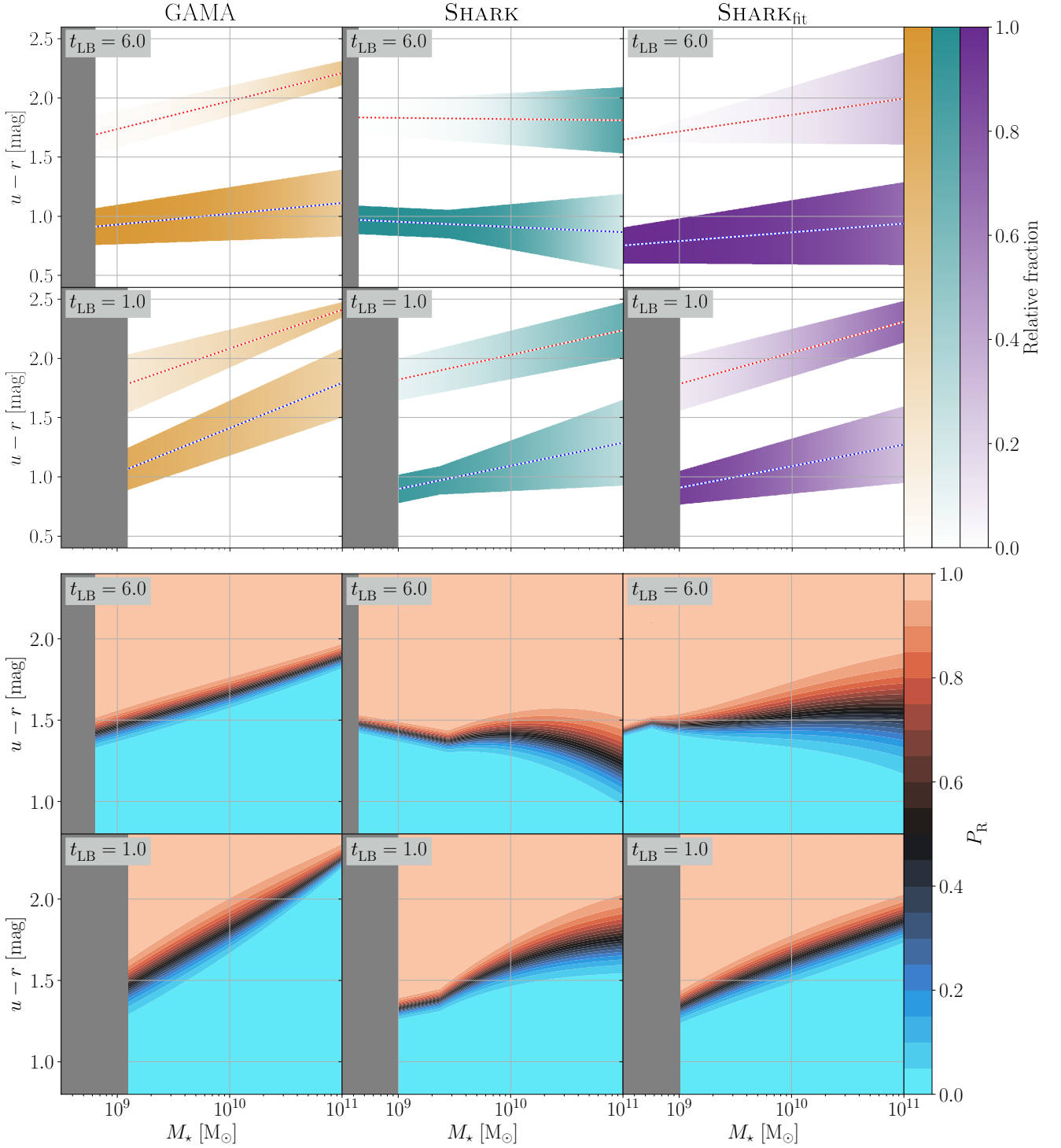


**Figure 11.** Top set of panels: Schematic representation of the evolution, drawn using the parameterisations presented in Section 3 (3.3 and 3.4 in particular). The tow row shows the populations at a lookback time of 6 Gyr, the bottom at 1 Gyr. Each column corresponds to one of our galaxy samples: GAMA (left, orange), SHARK (middle, cyan) and SHARK<sub>fit</sub> (right, purple). The lines indicate the mean of each population as a function of stellar mass (colour-coded by the population they trace, blue or red), the shaded areas the 1-sigma width of the population as a function of mass, and the opacity shows the relative contribution of each population to the full population at a given stellar mass (lighter colours indicating a smaller contribution). Bottom set of panels: Contour map of the probability for a galaxy of being red ( $P_R$ ), as a function of stellar mass, colour and time. Note the smaller range in  $u-r$  compared to the top group of panels, which is to highlight the transition zone. The grey-shaded areas in all panels indicate the mass completeness limit for each sample and lookback time. An animated version of this Figure is available in the supplemental material.

relatively small impact on SEDs, hence making early epochs poorly constrained. Another difference appears in the width of the blue population for the galaxies with  $M_{\star} \lesssim 10^{10} M_{\odot}$ , where GAMA and  $\text{SHARK}_{\text{fit}}$  show a larger scatter than SHARK. A naive expectation would be for the opposite, given the small number of free parameters involved in SED fitting compared to a SAM. This suggests that either our choice of priors are responsible, or the galaxy SEDs lack the constraining power to produce the narrow low-mass blue population seen in SHARK. This is also visible in Figure 3, where a wider variation in SFHs is seen in both GAMA and  $\text{SHARK}_{\text{fit}}$ .

In practice, this sets an upper limit for the trustworthiness of our reconstruction, which we estimate at  $t_{\text{LB}} \sim 6$  Gyr, given that SHARK and  $\text{SHARK}_{\text{fit}}$  are broadly similar up to that lookback time. This time limit will be used in our future work (Bravo et al. in preparation).

#### 4.1.2 (iii) How can we best define the blue and red populations across cosmic time?

We can fully describe the galaxy colour distribution in our three galaxy samples (GAMA, SHARK and  $\text{SHARK}_{\text{fit}}$ ) as a combination of two Gaussians. At a given stellar mass and time, the parameters of these Gaussians (means, weights and standard deviations) can be accurately described by simple functional forms with only two free parameters. For the means, this is not only in line with the well-established colour-magnitude relation for both early- and late-type galaxies (e.g., Baum et al. 1959; Faber 1973; Visvanathan & Sandage 1977; Bower et al. 1992), but also with the results shown for GAMA by T15 in the overlapping mass range. Also broadly aligned with T15 is our finding of linear relations between the width of the Gaussians and stellar mass. We, however, expand over previous work in showing that these results hold at earlier cosmic times as well as at  $z \sim 0$ .

Together the means and standard deviations produce a fairly simple description of the blue and red populations, as can be seen in the upper panels of Figure 11. The inclusion of weights in our modelling unlocks the more complex distribution of the probability of a galaxy being red that is seen in the bottom panels of Figure 11. These show that a statistically-driven selection of blue and red galaxies can not be replicated by the more simple selection criteria that are common in literature (e.g., Trayford et al. 2016; Nelson et al. 2018; Bremer et al. 2018; Wright et al. 2019). The latter is a fundamental aspect to consider when attempting to infer colour transition timescales (which we will consider in Bravo et al. in preparation).

#### 4.1.3 (iv) Is the green value a superposition of the blue and red populations, or a population on its own?

In agreement with the results from Schawinski et al. (2014) and T15, we do not find evidence for a separate green population at any cosmic time. Hence, the green valley is only a product of the overlap of the blue and red populations. The presence of this overlap between the blue and red populations indicates that galaxies become red before they reach a colour close to the mean of the red population, suggesting that the transformation from blue to red happens on shorter timescales than the transition from being confidently-classified as blue to confidently classified as red. It also indicates that blue galaxies can be considerably redder than the bluest galaxies of the red population. While that statement may seem contradictory, it points to an intrinsic difference between both populations that it is

not fully captured just by colour and stellar mass. This suggests that the processes that are responsible for transforming a blue galaxy into a red galaxy are not the same, or at least operate differently, to those that make a blue galaxy a comparatively red member of the blue population.

This poses a challenge for measuring transition timescales, as without additional information we can only ascertain the probability of a galaxy belonging to either population. While Schawinski et al. (2014) has shown that morphology does provide certainty for the blue/red classification, it is impractical for our purposes, as that would require a method to recover the morphological evolution of a galaxy, something outside the reach of anything but small, targeted integral field spectroscopy surveys. Still, much can be gained from the upper limit on the colour transition timescales that we can measure using the population description, which will be the aim of future work (Bravo et al. in preparation).

#### 4.1.4 (i) How have the colours of the local blue and red populations evolve with time?

The decrease of the transition mass ( $M_{\text{T}}$ ) from  $\sim 10^{10.9} M_{\odot}$  at 6 Gyr to  $\sim 10^{10.6} M_{\odot}$  at 1 Gyr means that the red population assembles at the high-mass end, extending into lower masses with time, in agreement with existing literature (e.g., Borch et al. 2006; Faber et al. 2007; Gonçalves et al. 2012). We also find that both blue and red massive galaxies become redder with time, while smaller galaxies remain a similar colour through cosmic time, in agreement with the cosmic SFH results in B20b (see their figure 7). These two results combined are consistent with the idea of downsizing (e.g., Cowie et al. 1996; Kodama et al. 2004; Neistein et al. 2006; Fontanot et al. 2009; Gonçalves et al. 2012). This suggests that small galaxies follow evolutionary paths that are not directly affected by the age of the Universe, while massive galaxies become noticeably more metal-rich, less star-forming, or a mix of both, with cosmic time. Another almost constant quantity with time is the width of the colour distribution of each population, which suggests that, for a given mass, the variety of evolutionary paths that galaxies follow to reach said mass is invariant with cosmic time. The sharpness of the transition from blue- to red-dominated decreases with time, which implies that the quenching timescale for galaxies near the transition mass becomes larger with time. At the low-mass end, the near static nature of both populations suggests the timescales are near time-invariant for these galaxies.

## 4.2 Extrapolating future galaxy colour evolution

If we assume galaxy colours continue to evolve as they have evolved in the past, we can speculatively make future predictions for the evolution of the galaxy populations. In particular, it is expected that current star-forming galaxies will eventually run out of gas, leaving only one (red) population in the far distant future. Extrapolating from our results we calculate at which time this will occur for a given stellar mass, i.e., when the blue and red populations overlap. This is shown in Figure 12 by calculating the time at which both red and blue populations have the same mean.

GAMA predicts a much faster rate of merging of the two populations than SHARK and  $\text{SHARK}_{\text{fit}}$ , which are in very good agreement with each other. For this reason, we will focus only on the extrapolation from GAMA, as it is based on observations and should offer better predictions. For example, an extrapolation of our trends suggests that all  $> 10^{10} M_{\odot}$  galaxies will be quenched by  $\sim 8$  Gyr.



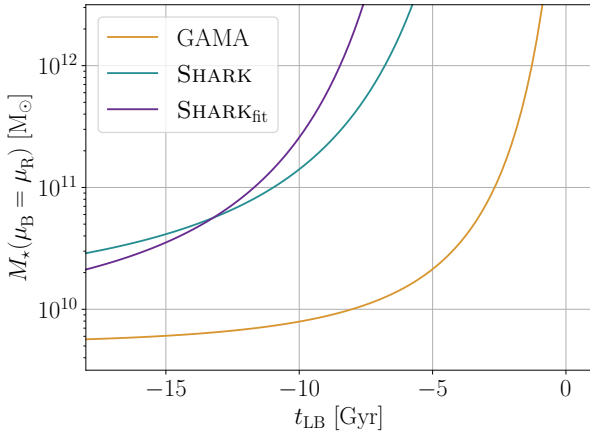


**Figure 12.** Stellar mass at which both populations are predicted to have the same mean value, as a function of time.

This speculative extrapolation also allows us to make predictions for Milky Way-like galaxies. A simple estimate for the timescale on which it will stop forming stars can be made by assuming a constant SFR and no further gas accretion (closed box). For the current SFR ( $1.65 \text{ M}_{\odot} \text{ yr}^{-1}$ , Licquia & Newman 2015) and gas mass ( $\text{HI} + \text{H}_2 = 1.05 \times 10^{10} \text{ M}_{\odot}$  Kalberla & Kerp 2009) values, this leads to an estimate of  $\sim 6$  Gyr. While this is longer than our prediction of  $\sim 3$  Gyr for the colour evolution of a  $10^{10.7} \text{ M}_{\odot}$  Milky Way-like galaxy (Licquia & Newman 2015), the simple estimate we present above ignores the effect of outflows, which would reduce the estimated timescale (and the difference with our prediction). While these extrapolations should be read with caution, the agreement in estimates for the Milky Way and consistency with galaxy downsizing are encouraging.

## 5 CONCLUSIONS

In this work we have introduced a novel method to reconstruct the colour evolution of low-redshift galaxies, using the SED fitting software ProSPECT. We then present a method to classify galaxies into colour populations and characterising their evolution in time. We test these methods using simulated galaxies from SHARK, testing both the predicted evolution from the simulation and how our reconstructing method matches the true evolution when the answer is known beforehand.

Our main findings can be summarised as:

- We can to reconstruct the evolution of galaxies up to a lookback time of  $\sim 6$  Gyr, from where our results become driven by the modelling choices we adopt for the SED fitting.
- We find no evidence of a green galaxy population, with the green valley being a mix of blue and red galaxies.
- While in good qualitative agreement, small but measurable tensions in the colour evolution of galaxies are apparent at the quantitative level between simulations and observations.
- At a fixed stellar mass, we observe a strong colour evolution for massive galaxies, both blue and red, while low-mass galaxies remain of a similar colour.
- We find that galaxies reaching a given stellar mass display a variety of evolutionary paths that is invariant with time, as en-

coded in the almost complete lack of evolution of the width of the populations.

- We find further evidence for the red population assembling from the high-mass end down.

These results will serve as the foundation for our future work (Bravo et al. in preparation), where we will use this statistical model of the colour population to select present-day red galaxies and study the timescales for their transition from blue to red galaxies.

## ACKNOWLEDGEMENTS

We thank Chris Power and Pascal Elahi for their role in completing the SURFS *N*-body DM-only simulations suite, Rodrigo Tobar for his contributions to SHARK, and the anonymous referee for their constructive report. MB acknowledges the support of the University of Western Australia through a Scholarship for International Research Fees and Ad Hoc Postgraduate Scholarship. LJMD and ASGR and LC acknowledge support from the Australian Research Councils Future Fellowship scheme (FT200100055 and FT200100375, respectively) CdPL is funded by the ARC Centre of Excellence for All Sky Astrophysics in 3 Dimensions (ASTRO 3D), through project number CE170100013. CdPL also thanks the MERAC Foundation for a Postdoctoral Research Award. SB acknowledges support by the Australian Research Council’s funding scheme DP180103740. JET is supported by the Australian Government Research Training Program (RTP) Scholarship.

This work was supported by resources provided by the Pawsey Supercomputing Centre with funding from the Australian Government and the Government of Western Australia. We gratefully acknowledge DUG Technology for their support and HPC services.

GAMA is a joint European-Australasian project based around a spectroscopic campaign using the Anglo-Australian Telescope. The GAMA input catalogue is based on data taken from the Sloan Digital Sky Survey and the UKIRT Infrared Deep Sky Survey. Complementary imaging of the GAMA regions is being obtained by a number of independent survey programmes including GALEX MIS, VST KiDS, VISTA VIKING, WISE, Herschel-ATLAS, GMRT and ASKAP providing UV to radio coverage. GAMA is funded by the STFC (UK), the ARC (Australia), the AAO, and the participating institutions. The GAMA website is <http://www.gama-survey.org/>. Based on observations made with ESO Telescopes at the La Silla Paranal Observatory under programme ID 179.A-2004. Based on observations made with ESO Telescopes at the La Silla Paranal Observatory under programme ID 177.A-3016.

The analysis on this work was performed using the programming languages PYTHON v3.8 (<https://www.python.org>) and R v4.0 (<https://www.r-project.org>), with the open source libraries CELESTIAL (Robotham 2016), DATA.TABLE (<https://github.com/Rdatatable/data.table>), FOREACH (<https://github.com/RevolutionAnalytics/foreach>), MATPLOTLIB (Hunter 2007), MIXTOOLS (Benaglia et al. 2009), NUMPY (Harris et al. 2020), PANDAS (McKinney 2010), SCICM (<https://github.com/MBravoS/scicm>), and SCIPY (Virtanen et al. 2020), in addition of the software previously described.

## DATA AVAILABILITY

The SED fitting data from GAMA was provided by Sabine Bellstedt by permission, and will be shared on request to the corresponding

author with permission of Sabine Bellstedt. The SHARK simulated SEDs and SFH/ZH were produced by the SHARK team for this work, and will be shared on reasonable request to the corresponding author. The PROSPECT fits to SHARK galaxies and all reconstructed colour evolution tracks generated for this work will be shared on reasonable request to the corresponding author.

## REFERENCES

- Amarantidis S., et al., 2019, *MNRAS*, **485**, 2694
- Anghopo J., Ferreras I., Silk J., 2019, *MNRAS*, **488**, L99
- Arnaboldi M., Neeser M. J., Parker L. C., Rosati P., Lombardi M., Dietrich J. P., Hummel W., 2007, *The Messenger*, **127**, 28
- Baldry I. K., Glazebrook K., Brinkmann J., Ivezić Ž., Lupton R. H., Nichol R. C., Szalay A. S., 2004, *ApJ*, **600**, 681
- Baldry I. K., Balogh M. L., Bower R. G., Glazebrook K., Nichol R. C., Bamford S. P., Budavari T., 2006, *MNRAS*, **373**, 469
- Baldry I. K., et al., 2014, *MNRAS*, **441**, 2440
- Balogh M. L., Navarro J. F., Morris S. L., 2000, *ApJ*, **540**, 113
- Barro G., et al., 2013, *ApJ*, **765**, 104
- Baum W. A., Hiltner W. A., Johnson H. L., Sandage A. R., 1959, *ApJ*, **130**, 749
- Bell E. F., McIntosh D. H., Katz N., Weinberg M. D., 2003, *ApJS*, **149**, 289
- Bell E. F., et al., 2004, *ApJ*, **608**, 752
- Belli S., Newman A. B., Ellis R. S., 2015, *ApJ*, **799**, 206
- Belli S., Newman A. B., Ellis R. S., 2019, *ApJ*, **874**, 17
- Belli S., et al., 2021, *ApJ*, **909**, L11
- Bellstedt S., et al., 2020a, *MNRAS*, **496**, 3235
- Bellstedt S., et al., 2020b, *MNRAS*, **498**, 5581
- Bellstedt S., et al., 2021, *MNRAS*, **503**, 3309
- Benaglia T., Chauveau D., Hunter D. R., Young D., 2009, *Journal of Statistical Software*, **32**, 1
- Blanton M. R., 2006, *ApJ*, **648**, 268
- Blanton M. R., et al., 2003, *ApJ*, **594**, 186
- Boquien M., Burgarella D., Roehlly Y., Buat V., Ciesla L., Corre D., Inoue A. K., Salas H., 2019, *A&A*, **622**, A103
- Borch A., et al., 2006, *A&A*, **453**, 869
- Bower R. G., Lucey J. R., Ellis R. S., 1992, *MNRAS*, **254**, 601
- Bower R. G., Benson A. J., Malbon R., Helly J. C., Frenk C. S., Baugh C. M., Cole S., Lacey C. G., 2006, *MNRAS*, **370**, 645
- Bravo M., Lagos C. d. P., Robotham A. S. G., Bellstedt S., Obreschkow D., 2020, *MNRAS*, **497**, 3026
- Bremer M. N., et al., 2018, *MNRAS*, **476**, 12
- Brown J. S., Martini P., Andrews B. H., 2016, *MNRAS*, **458**, 1529
- Brown T., Cortese L., Catinella B., Kilborn V., 2018, *MNRAS*, **473**, 1868
- Bruzual G., Charlot S., 2003, *MNRAS*, **344**, 1000
- Cañas R., Elahi P. J., Welker C., del P Lagos C., Power C., Dubois Y., Pichon C., 2019, *MNRAS*, **482**, 2039
- Carnall A. C., McLure R. J., Dunlop J. S., Davé R., 2018, *MNRAS*, **480**, 4379
- Chabrier G., 2003, *PASP*, **115**, 763
- Charlot S., Fall S. M., 2000, *ApJ*, **539**, 718
- Chauhan G., Lagos C. d. P., Obreschkow D., Power C., Oman K., Elahi P. J., 2019, *MNRAS*, **488**, 5898
- Chauhan G., Lagos C. d. P., Stevens A. R. H., Obreschkow D., Power C., Meyer M., 2020, *MNRAS*, **498**, 44
- Chauhan G., Lagos C. d. P., Stevens A. R. H., Bravo M., Rhee J., Power C., Obreschkow D., Meyer M., 2021, *arXiv e-prints*, [p. arXiv:2102.12203](https://arxiv.org/abs/2102.12203)
- Chevallard J., Charlot S., 2016, *MNRAS*, **462**, 1415
- Cowie L. L., Songaila A., Hu E. M., Cohen J. G., 1996, *AJ*, **112**, 839
- Croton D. J., et al., 2006, *MNRAS*, **365**, 11
- Crowl H. H., Kenney J. D. P., van Gorkom J. H., Vollmer B., 2005, *AJ*, **130**, 65
- Dale D. A., Helou G., Magdis G. E., Armus L., Díaz-Santos T., Shi Y., 2014, *ApJ*, **784**, 83
- Dalla Vecchia C., Schaye J., 2012, *MNRAS*, **426**, 140
- Davies L. J. M., et al., 2019a, *MNRAS*, **483**, 1881
- Davies L. J. M., et al., 2019b, *MNRAS*, **483**, 5444
- Dekel A., Birnboim Y., 2006, *MNRAS*, **368**, 2
- Driver S. P., et al., 2006, *MNRAS*, **368**, 414
- Driver S. P., et al., 2011, *MNRAS*, **413**, 971
- Elahi P. J., Power C., Lagos C. d. P., Poulton R., Robotham A. S. G., 2018, *MNRAS*, **477**, 616
- Elahi P. J., Cañas R., Poulton R. J. J., Tobar R. J., Willis J. S., Lagos C. d. P., Power C., Robotham A. S. G., 2019a, *Publ. Astron. Soc. Australia*, **36**, e021
- Elahi P. J., Poulton R. J. J., Tobar R. J., Cañas R., Lagos C. d. P., Power C., Robotham A. S. G., 2019b, *Publ. Astron. Soc. Australia*, **36**, e028
- Faber S. M., 1973, *ApJ*, **179**, 731
- Faber S. M., et al., 2007, *ApJ*, **665**, 265
- Fang J. J., Faber S. M., Koo D. C., Dekel A., 2013, *ApJ*, **776**, 63
- Feltre A., Hatziminaoglou E., Fritz J., Franceschini A., 2012, *MNRAS*, **426**, 120
- Fontanot F., De Lucia G., Monaco P., Somerville R. S., Santini P., 2009, *MNRAS*, **397**, 1776
- Fossati M., et al., 2017, *ApJ*, **835**, 153
- Fritz J., Franceschini A., Hatziminaoglou E., 2006, *MNRAS*, **366**, 767
- Gonçalves T. S., Martin D. C., Menéndez-Delmestre K., Wyder T. K., Koekemoer A., 2012, *ApJ*, **759**, 67
- Hahn C., Tinker J. L., Wetzel A., 2017, *ApJ*, **841**, 6
- Han Y., Han Z., 2014, *ApJS*, **215**, 2
- Harris C. R., et al., 2020, *Nature*, **585**, 357
- Hogg D. W., et al., 2002, *AJ*, **124**, 646
- Hopkins P. F., Hernquist L., Cox T. J., Di Matteo T., Robertson B., Springel V., 2006, *ApJS*, **163**, 1
- Hunter J. D., 2007, *Computing In Science & Engineering*, **9**, 90
- Iyer K., Gawiser E., 2017, *ApJ*, **838**, 127
- Kalberla P. M. W., Kerp J., 2009, *ARA&A*, **47**, 27
- Kalinova V., Colombo D., Sánchez S. F., Kodaira K., García-Benito R., González Delgado R., Rosolowsky E., Lacerda E. A. D., 2021, *A&A*, **648**, A64
- Katsianis A., et al., 2019, *ApJ*, **879**, 11
- Kauffmann G., White S. D. M., Heckman T. M., Ménard B., Brinchmann J., Charlot S., Tremonti C., Brinkmann J., 2004, *MNRAS*, **353**, 713
- Kaviraj S., Devriendt J. E. G., Ferreras I., Yi S. K., Silk J., 2009, *A&A*, **503**, 445
- Kawata D., Mulchaey J. S., 2008, *ApJ*, **672**, L103
- Kereš D., Katz N., Weinberg D. H., Davé R., 2005, *MNRAS*, **363**, 2
- Kodama T., et al., 2004, *MNRAS*, **350**, 1005
- Kroupa P., 2001, *MNRAS*, **322**, 231
- Lagos C. d. P., Lacey C. G., Baugh C. M., 2013, *MNRAS*, **436**, 1787
- Lagos C. d. P., Tobar R. J., Robotham A. S. G., Obreschkow D., Mitchell P. D., Power C., Elahi P. J., 2018, *MNRAS*, **481**, 3573
- Lagos C. d. P., et al., 2019, *MNRAS*, **489**, 4196
- Lagos C. d. P., da Cunha E., Robotham A. S. G., Obreschkow D., Valentino F., Fujimoto S., Magdis G. E., Tobar R., 2020, *arXiv e-prints*, [p. arXiv:2007.09853](https://arxiv.org/abs/2007.09853)
- Lara-López M. A., et al., 2010, *A&A*, **521**, L53
- Lara-López M. A., López-Sánchez Á. R., Hopkins A. M., 2013, *ApJ*, **764**, 178
- Leja J., Johnson B. D., Conroy C., van Dokkum P. G., Byler N., 2017, *ApJ*, **837**, 170
- Lewis I. J., et al., 2002, *MNRAS*, **333**, 279
- Licquia T. C., Newman J. A., 2015, *ApJ*, **806**, 96
- Liske J., et al., 2015, *MNRAS*, **452**, 2087
- Machacek M., Jones C., Forman W. R., Nulsen P., 2006, *ApJ*, **644**, 155
- Mannucci F., Cresci G., Maiolino R., Marconi A., Gnerucci A., 2010, *MNRAS*, **408**, 2115
- Martin D. C., et al., 2005, *ApJ*, **619**, L1
- Martin D. C., et al., 2007, *ApJS*, **173**, 342
- McCarthy I. G., Frenk C. S., Font A. S., Lacey C. G., Bower R. G., Mitchell N. L., Balogh M. L., Theuns T., 2008, *MNRAS*, **383**, 593
- McKinney W., 2010, in van der Walt S., Millman J., eds, *Proceedings of the 9th Python in Science Conference*. pp 51 – 56

Moustakas J., et al., 2013, *ApJ*, **767**, 50

Neistein E., van den Bosch F. C., Dekel A., 2006, *MNRAS*, **372**, 933

Nelson D., et al., 2018, *MNRAS*, **475**, 624

Noll S., Burgarella D., Giovannoli E., Buat V., Marcellac D., Muñoz-Mateos J. C., 2009, *A&A*, **507**, 1793

Peng Y.-j., et al., 2010, *ApJ*, **721**, 193

Peng Y., Maiolino R., Cochrane R., 2015, *Nature*, **521**, 192

Pilbratt G. L., et al., 2010, *A&A*, **518**, L1

Planck Collaboration et al., 2016, *A&A*, **594**, A13

Poulton R. J. J., Robotham A. S. G., Power C., Elahi P. J., 2018, *Publ. Astron. Soc. Australia*, **35**, 42

Rémy-Ruyer A., et al., 2014, *A&A*, **563**, A31

Robotham A. S. G., 2016, *Celestial: Common astronomical conversion routines and functions* (ascl:1602.011)

Robotham A. S. G., Davies L. J. M., Driver S. P., Koushan S., Taranu D. S., Casura S., Liske J., 2018, *MNRAS*, **476**, 3137

Robotham A. S. G., Bellstedt S., Lagos C. d. P., Thorne J. E., Davies L. J., Driver S. P., Bravo M., 2020, *MNRAS*, **495**, 905

Saunders W., et al., 2004, in Moorwood A. F. M., Iye M., eds, *Society of Photo-Optical Instrumentation Engineers (SPIE) Conference Series* Vol. 5492, *Ground-based Instrumentation for Astronomy*. pp 389–400, doi:10.1117/12.550871

Schaller G., Schaerer D., Meynet G., Maeder A., 1992, *A&AS*, **96**, 269

Schawinski K., et al., 2014, *MNRAS*, **440**, 889

Schechter P., 1976, *ApJ*, **203**, 297

Sharp R., et al., 2006, in *Society of Photo-Optical Instrumentation Engineers (SPIE) Conference Series*. p. 62690G (arXiv:astro-ph/0606137), doi:10.1117/12.671022

Smethurst R. J., et al., 2018, *MNRAS*, **473**, 2679

Somerville R. S., Hopkins P. F., Cox T. J., Robertson B. E., Hernquist L., 2008, *MNRAS*, **391**, 481

Springel V., Di Matteo T., Hernquist L., 2005, *MNRAS*, **361**, 776

Strateva I., et al., 2001, *AJ*, **122**, 1861

Sutherland W., et al., 2015, *A&A*, **575**, A25

Taylor E. N., et al., 2015, *MNRAS*, **446**, 2144

Thorne J. E., et al., 2021, *MNRAS*,

Trayford J. W., Theuns T., Bower R. G., Crain R. A., Lagos C. d. P., Schaller M., Schaye J., 2016, *MNRAS*, **460**, 3925

Trayford J. W., Lagos C. d. P., Robotham A. S. G., Obreschkow D., 2020, *MNRAS*, **491**, 3937

Trussler J., Maiolino R., Maraston C., Peng Y., Thomas D., Goddard D., Lian J., 2020, *MNRAS*, **491**, 5406

Vazdekis A., Koleva M., Ricciardelli E., Röck B., Falcón-Barroso J., 2016, *MNRAS*, **463**, 3409

Virtanen P., et al., 2020, *Nature Methods*, **17**, 261

Visvanathan N., Sandage A., 1977, *ApJ*, **216**, 214

Wetzel A. R., Tinker J. L., Conroy C., van den Bosch F. C., 2013, *MNRAS*, **432**, 336

Wheeler C., Phillips J. I., Cooper M. C., Boylan-Kolchin M., Bullock J. S., 2014, *MNRAS*, **442**, 1396

Wild V., et al., 2020, *MNRAS*, **494**, 529

Williams R. J., Quadri R. F., Franx M., van Dokkum P., Labbé I., 2009, *ApJ*, **691**, 1879

Wolf C., Meisenheimer K., Rix H. W., Borch A., Dye S., Kleinheinrich M., 2003, *A&A*, **401**, 73

Wright E. L., et al., 2010, *AJ*, **140**, 1868

Wright R. J., Lagos C. d. P., Davies L. J. M., Power C., Trayford J. W., Wong O. I., 2019, *MNRAS*, **487**, 3740

Wyder T. K., et al., 2007, *ApJS*, **173**, 293

Yesuf H. M., Faber S. M., Trump J. R., Koo D. C., Fang J. J., Liu F. S., Wild V., Hayward C. C., 2014, *ApJ*, **792**, 84

Zhang C., et al., 2021, *ApJ*, **911**, 57

da Cunha E., Charlot S., Elbaz D., 2008, *MNRAS*, **388**, 1595

van Dokkum P. G., Franx M., 1996, *MNRAS*, **281**, 985

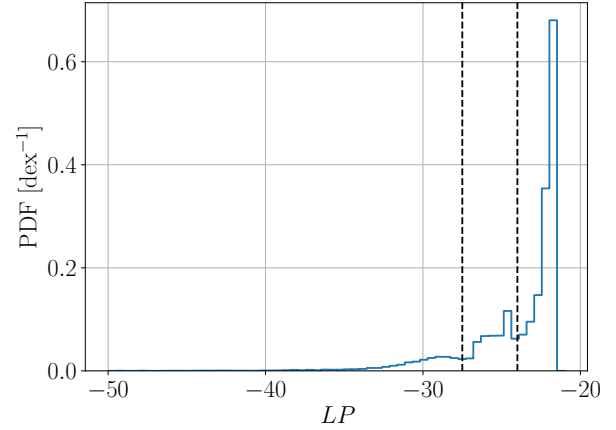


**Figure A1.** log-likelihood distribution of the SED fits to our SHARK galaxy sample. The two vertical lines (at  $LP = -24$  and  $LP = -27.5$ ) are used to divide the distribution in three regions for the following analysis. 65.7% of the galaxies have  $LP > -24$ , 22.1% lie in the intermediate region and 12.2% are below  $-27.5$ .

## APPENDIX A: PROSPECT FIT OF SHARK GALAXIES

As discussed in Section 2.3, we found that the results of our PROSPECT SED fits to SHARK galaxies lead to a different stacked star formation history. This is displayed by the solid lines in Figure A2, showing that, while recovering the correct peak of star formation, the recovered stacked SFH is flatter than in SHARK. Unlike the fits to observations done by B20b and Thorne et al. (2021), we find that the distribution of the log-likelihood of our fits (Figure A1) is not monotonically increasing, but show clear over-dense regions below the peak of the distribution. This suggests that, either by our choices on how to fit the galaxies or intrinsic properties of SHARK galaxies, some of the galaxies are harder to fit.

Splitting the galaxy sample by log-likelihood (the vertical dotted lines in Figure A1) into three reveals three distinct evolutionary paths (segmented lines in Figure A2). Not surprisingly, the best fit population has the highest contribution to the stacked SFH at late times ( $t_{LB} \leq 6$  Gyr), with the other two driving the peak in the SFH. More interesting is that in all three populations the SHARK<sub>fit</sub> stacked SFH exhibit different issues. The best-fit galaxies are slightly biased toward more recent star formation, those in the log-likelihood middle region show a significantly slower and smaller evolution of the SFH, being the main reason for the missing star formation around the peak, and the tail of the distribution shows a strong over-prediction at  $\sim 2.5$ -5 Gyr. Furthermore, from the galaxy properties in SHARK, we find that each of these populations splits naturally into two, by different properties each (though all linked to some degree to gas-phase metallicity), as shown in Figure A3. Note that for the populations in the tail-end we will use the terms "blue" and "red" (in quotes) to highlight that this is a far less rigorous definition than the one we use in the main body of this work.

As the unobscured view into the stellar population of dust-poor star-forming galaxies (blue lines, top panel of Figure A3) makes them the simplest target for SED fitting, that they show a superb match in SFH is unremarkable. While the recent/ongoing star formation in galaxies with more dust attenuation (orange lines, top panel of Figure A3) translates into a strong anchor for the SED fit, it reduces the constraining power for early star formation. In

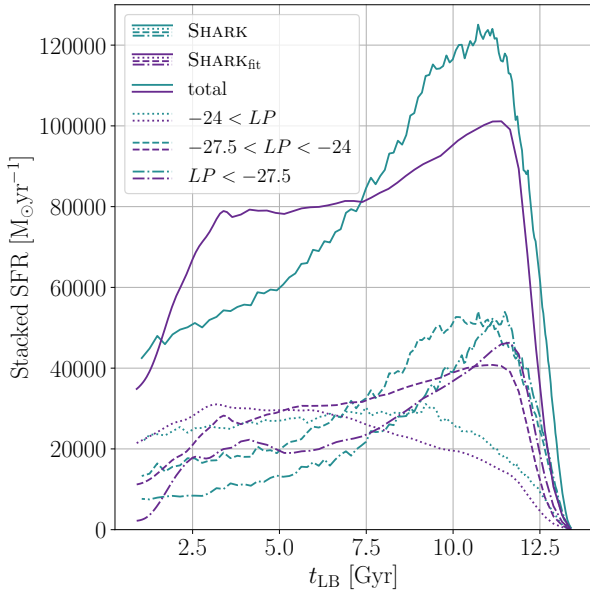


**Figure A2.** Comparison of stacked SFH of our SHARK sample (cyan lines) to the SFH from the SED fit with ProSPECT to these galaxies (purple lines). Solid lines show the total stacked SFH, dotted lines show for galaxies with  $LP > -24$ , dashed for galaxies with  $-27.5 < LP < -24$  and dash-dotted lines for  $LP < -27.5$ .

galaxies with a more complex SFH, this can lead to poor recovery of the early star formation, while still providing a good match to the SED across all bands.

The high-metallicity galaxies in the log-likelihood middle region (purple lines, middle panel of Figure A3), which are characterised by multiple massive bursts in star formation, make for some of the most challenging SHARK galaxies to fit. This is mainly due to our choice of SFH parameterisation, which is unable to reproduce the highly variable SFH that these galaxies exhibit, which leads to a flatter SFH. A by-product of their complex SFHs is that they reach gas-phase metallicity values near or above the GALAXEV template limit ( $Z = 0.005$ ) before having built most of their stellar mass, which means that these galaxies have access to old metal-rich stellar templates. In contrast, our choice of prior for  $Z_{\text{final}}$  means that we only allow for such high metallicities (and hence metal-rich templates) only near the end of the mass build-up. This is also the main driver for the weakly flatter SFH seen in poor-fitted "blue" galaxies (brown lines, bottom panel of Figure A3).

For the remaining two groups of galaxies, the culprit seems to be a mix of our choice of errors and priors for the fitting. This combination leads to a fast convergence to a reasonable SED fit with the lowest  $M_{\text{period}}$  we allow, but an extremely large cost to move a solution that more closely matches the true SFH. We have tested different error budgets, both fixed SNR (from 2 to 20% of the flux) and variable by band (drawing from the reported photometric errors Bellstedt et al. 2020a), and found the choice presented in the main body to produce the best recovery of the stacked SFH. We also tested the  $m_{\text{period}}$  used by Thorne et al. (2021)<sup>12</sup> but found that it penalises low values too strongly, leading to a recovered stacked

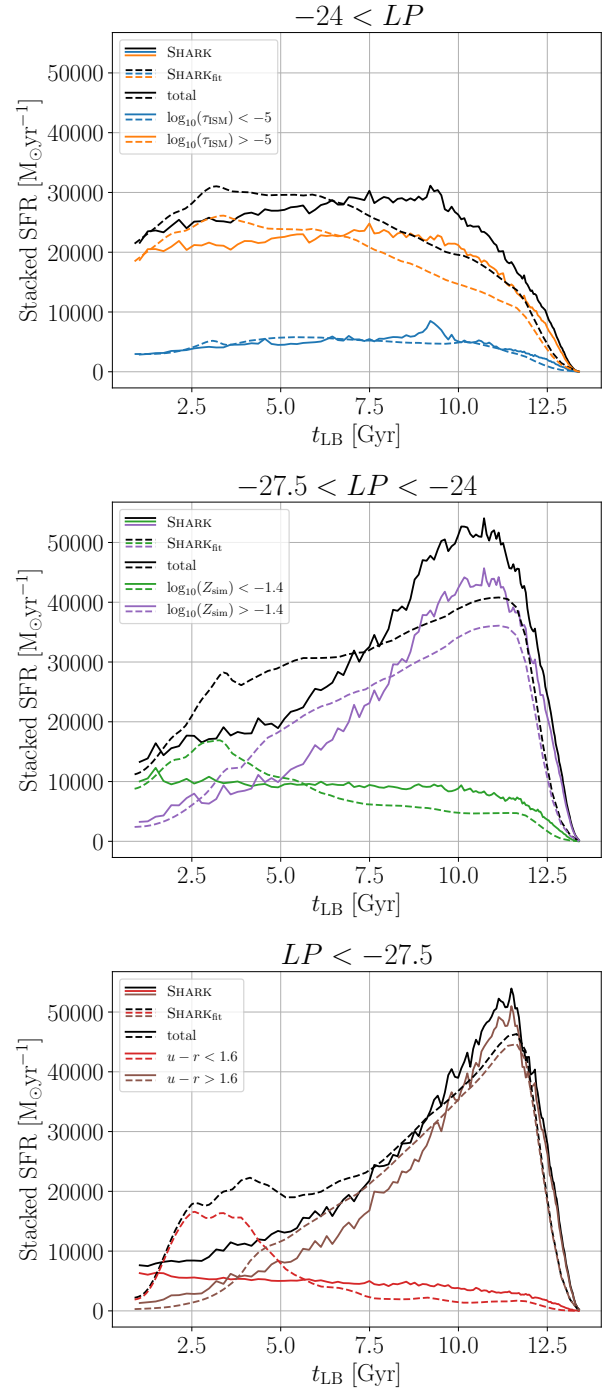


**Figure A3.** Stacked SFHs for each  $LP$  range, divided by the two most obvious populations in each. The top panel shows the SFH for galaxies with  $LP > -24$ , divided by the mass-weighted opacity of ISM in SHARK (46.3% above and 19.4% below). The middle shows the SFH for the  $-27.5 < LP < -24$  range, divided by the gas metallicity of the galaxies (6.2% and 15.9%). The bottom shows the SFH for galaxies below  $LP = -27.5$ , divided by intrinsic galaxy colour (3.7% and 8.5%).

<sup>12</sup> The prior equation is  $100(\text{erf}(M_{\text{period}} + 2) - 1)$ , as described in table 1 from Thorne et al. (2021)



GAMA	$x_{2yz}$	$x_{1yz}$	$x_{0yz}$
$\alpha_{\mu B}$	$7.0133 \times 10^{-3}$	$-1.0716 \times 10^{-1}$	$4.8142 \times 10^{-1}$
$\beta_{\mu B}$	$4.8100 \times 10^{-3}$	$-1.4081 \times 10^{-1}$	$1.7386 \times 10^0$
$\alpha_{\mu R}$	$0 \times 10^0$	$-1.8180 \times 10^{-2}$	$3.4574 \times 10^{-1}$
$\beta_{\mu R}$	$0 \times 10^0$	$-3.1144 \times 10^{-2}$	$2.2782 \times 10^0$
$M_T$	$1.1432 \times 10^{-2}$	$1.4103 \times 10^{-1}$	$1.0514 \times 10^1$
$k$	$0 \times 10^0$	$1.9138 \times 10^{-1}$	$6.8639 \times 10^{-1}$
$\alpha_{\sigma B}$	$1.3935 \times 10^{-3}$	$-1.0015 \times 10^{-2}$	$6.8116 \times 10^{-2}$
$\beta_{\sigma B}$	$-6.6184 \times 10^{-4}$	$2.9764 \times 10^{-3}$	$2.6013 \times 10^{-1}$
$\alpha_{\sigma R}$	$-2.3998 \times 10^{-3}$	$3.0898 \times 10^{-2}$	$-1.2431 \times 10^{-1}$
$\beta_{\sigma R}$	$1.9837 \times 10^{-4}$	$-6.7682 \times 10^{-4}$	$1.1301 \times 10^{-1}$
SHARK	$x_{2yz}$	$x_{1yz}$	$x_{0yz}$
$\alpha_{\mu B}$	$4.6957 \times 10^{-3}$	$-8.0686 \times 10^{-2}$	$2.7111 \times 10^{-1}$
$\beta_{\mu B}$	$2.3864 \times 10^{-3}$	$-7.7312 \times 10^{-2}$	$1.2660 \times 10^0$
$\alpha_{\mu R}$	$0 \times 10^0$	$-4.3754 \times 10^{-2}$	$2.5236 \times 10^{-1}$
$\beta_{\mu R}$	$0 \times 10^0$	$-6.3653 \times 10^{-2}$	$2.1977 \times 10^0$
$M_T$	$5.0981 \times 10^{-1}$	$-5.3681 \times 10^0$	$1.0445 \times 10^1$
$k$	$-3.4632 \times 10^{-2}$	$5.2733 \times 10^{-1}$	$1.0014 \times 10^0$
$\alpha_{\sigma B}$	$-5.1590 \times 10^{-5}$	$-3.2870 \times 10^{-3}$	$1.5234 \times 10^{-1}$
$\beta_{\sigma B}$	$1.2420 \times 10^{-3}$	$-1.4855 \times 10^{-2}$	$3.0219 \times 10^{-1}$
$\alpha_{\sigma R}$	$1.0477 \times 10^{-3}$	$-9.7242 \times 10^{-4}$	$2.7621 \times 10^{-2}$
$\beta_{\sigma R}$	$8.6397 \times 10^{-4}$	$1.0818 \times 10^{-4}$	$2.1788 \times 10^{-1}$

**Table B1.** Values for the time evolution parameterisation of the means (Section 3.3.1, Equations 6-7), weights (Section 3.4.1, Equations 12-15) and standard deviations (Section 3.4.2, Equations 18-21).

SFH flatter than in SHARK, driven by poor fits to the SHARKgalaxies that display such short periods of star formation.

## APPENDIX B: TABULATED EVOLUTION PARAMETERS

Table B1 shows the best fit parameters for Equations 6, 7, 8, 9, 12, 13, 14, 15, 18, 19, 20 and 21.

This paper has been typeset from a  $\text{\LaTeX}$  file prepared by the author.